(A New Proposal to Jefferson Lab PAC21)

Measurement of the Neutron Electric Form Factor G_{En} at High Q^2

J. P. Chen, E. Chudakov, C. DeJager, P. Degtyarenko, J. Gomez, O. Hansen,
D. W. Higinbotham, M. Jones, J. LeRose, W. Melnitchouk, R. Michaels, S. Nanda,
B. Reitz (spokesperson), A. Saha, B. Wojtsekhowski (spokesperson and contact person), S. Wood
Thomas Jefferson National Accelerator Facility, Newport News, VA 23606

B. Anderson, A.T. Katramatou, K. McCormick (spokesperson),
G.G. Petratos, J. Watson, Wei-Ming Zhang
Kent State University, Kent, OH 44242

G. Cates (spokesperson), D. Day, A. Deur, R. Lindgren, N. Liyanage,
V. Nelyubin†, B. E. Norum, K. Wang
University of Virginia, Charlottesville, VA 22901

G. Warren
University of Basel, Basel, Switzerland

D. Nikolenko, I. Rachek
Budker Institute, Novosibirsk, Russia

J. Annand, D. Ireland, J. Kellie, K. Livingston, G. Rosner, D. Watts
University of Glasgow, Glasgow, Scotland

P. Markowitz, M. M. Sargsian
Florida International University, Miami, FL 33199

A. Danagoulian, A. Nathan
University of Illinois, Champaign-Urbana, IL 61801

W. Korsch, P. Zolnierczuk
The University of Kentucky, Lexington, KY 40506

K.G. Fissum
University of Lund, Lund, Sweden

J. M. Udias
Universidad Complutense de Madrid, Madrid, Spain

J. J. Kelly
University of Maryland, College Park, MD 20292

J. Calarco, W. Hersman
University of New Hampshire, Durham, NH 03824

V. Punjabi
Norfolk State University, Norfolk, VA 23504

B. Vlahovic
North Carolina Central University, Durham, NC 03824

R. Niyazov, A. Radyushkin, L. Weinstein
Old Dominion University, Norfolk, VA 23529

M. Strikman
Pennsylvania State University, University Park, PA 16802

P. Stoler
Rensselaer Polytechnic Institute,Troy, NY 12180-3590

R. Gilman, C. Glashausser, X. Jiang, G. Kumbartzki, R. Ransome
Rutgers, The State University of New Jersey, Piscataway, NJ 08854

J. M. Laget, F. Sabatie
CEA Saclay, Gif-sur-Yvette, France

F. Garibaldi, M. Iodice
INFN, Rome, Italy

R. De Leo
INFN, Bari, Italy

J. Lichtenstadt, E. Piasetzky
Tel Aviv University, Israel

Seonho Choi, A. Lukhanin, Z.-E. Meziani, N. Ploquin, K. Slifer, P. Solvignon.
Temple University, Philadelphia, PA 19122

D. Armstrong, T. Averett, M. Finn, C. Perdrisat
College of William and Mary, Williamsburg, VA 23185

K. Egiyan, A. Ketikyan, A. Shahinyan, H. Voskanyan
Yerevan Physics Institute, Yerevan, Armenia

and
The Hall A Collaboration

† on leave from SPNPI of Russian Academy of Sciences, Gatchina, Russia

December 3, 2001

Abstract

We propose a measurement of the neutron electric form factor G_{En} at high four–momentum transfer values of $Q^2 = 1.3$, 2.4, and 3.4 $(\mathrm{GeV/c})^2$ in double polarized semi-exclusive $^3\vec{H}e(\vec{e}, e'n)$ scattering in quasi–elastic kinematics by measuring the asymmetry A_T of the cross section.

Results from the recent JLab experiment E93-027 for elastic electron-proton scattering, using a recoil polarization technique, show remarkable features for the proton electric form factor at these momentum transfers, whereas no accurate data on G_{En} are available.

The recently developed approach for calculations of exclusive reactions in the Q^2-range between 1 and 10 $(\mathrm{GeV/c})^2$ using generalized parton distributions (GPD) relates these elastic form factors to the results from deep inelastic scattering and from Compton scattering. Data for G_{En} at high Q^2 are necessary, in particular, to constrain spin-flip GPDs.

The experiment utilizes the polarized ^{3}He target and the polarized CEBAF beam at moderate beam energies of 1.644, 2.444, and 3.244 GeV. The electrons will be detected in the BigBite spectrometer, the neutrons in an array of scintillators. Because of the high kinetic energy of the neutrons, a high neutron detection efficiency with an excellent background suppression can be achieved.

Within 768 hours of beamtime G_{En} can be measured to a statistical accuracy of $\Delta G_{En}/G_{En}= 0.14$ for these three values of Q^2. Such a measurement would significantly increase our knowledge about a fundamental property of the neutron in a region where no accurate data are yet available.

1 Introduction

Knowledge of the neutron electric form factor G_{En} is essential for an understanding of nucleon structure. Furthermore it is an ingredient in the analysis of processes involving electromagnetic interactions with complex nuclei. The neutron electric form factor is related to the charge distribution of the valence and sea quarks inside the neutron. In the Breit–frame, where the squared three momentum transfer $\vec{q}^{\,2}$ equals the square of the four momentum transfer Q^2, G_{En} is the Fourier transform of the charge distribution. Such a Fourier transformation using the world data on the Sachs form factors has been done recently [1].

Recent surprising results on G_{Ep}, the electric form factor of the proton, from JLab experiments E93-027 and E99-007, utilizing a recoil polarization technique, show that the ratio G_{Ep}/G_{Mp} declines sharply as Q^2 increases, and therefore that the electric and magnetic form factors behave differently starting at $Q^2 \approx 1$ (GeV/c)^2 [2, 3]. The same mechanisms causing this deviation should also be present in the neutron. It is an intriguing question, how the ratio G_{En}/G_{Mn} develops in this Q^2 regime, where confinement plays an important role.

Our knowledge of G_{En} at high Q^2 is rather poor compared to the data available on the Sachs form factors of the proton, G_{Ep} and G_{Mp}, as well as on the neutron magnetic form factor G_{Mn}. The reason is twofold. Because the net charge of the neutron is zero, G_{En} is a very small quantity at low Q^2. Secondly, there are no free neutron targets on which to perform experiments.

Thermal–neutron scattering from atoms measures very precisely the RMS charge radius and the slope of $G_{En}(Q^2)$ at Q^2=0 [4, 5]. The slope of $G_{En}(Q^2)$ turns out to be positive at Q^2=0, leading to a RMS charge radius of -0.113 fm^2. Because the net charge of the neutron is zero, it therefore consists of a positive core surrounded by a negative cloud. There are a number of physical mechanisms which have been proposed to explain the origin of the neutron's charge distribution. The classical interpretation was in terms of a virtual negatively charged pion cloud surrounding a positively charged proton core. More recently, the idea emerged that the color-magnetic force associated with one gluon exchange between the valence quarks provides a repulsive force between pairs of d quarks, while causing attraction between u and d quarks. On average, therefore, the negatively charged d quarks are found further away from the center of the neutron than the positively charged u quarks, leading to the observed charged distribution. Which of these pictures provides the more accurate description is as yet unclear, and requires high precision data on G_{En} over a large range of Q^2.

Measuring G_{En} in inclusive unpolarized electron scattering is limited in the accuracy of the information it can provide. The standard method of the Rosenbluth separation is very demanding, for several reasons. Because $\tau G_{Mn} \gg G_{En}$ the magnetic form factor dominates the cross section. Additionally, these experiments have to be performed on light nuclei, mostly ^{2}H, so the contribution from the proton to the cross section has to be subtracted. Furthermore to extract the neutron information, the wave functions have to be known, and FSI, MEC, IC, and relativistic effects have to be taken into account. Results for G_{En} determined in quasi elastic $e-d$ scattering [6] are shown in Figure 1. The uncertainties are rather large, and the result is compatible with $G_{En}=0$, as well as with the Galster "parameterization", an empirical fit to data on G_{En} obtained at lower values of Q^2 [7]: G_{En}=

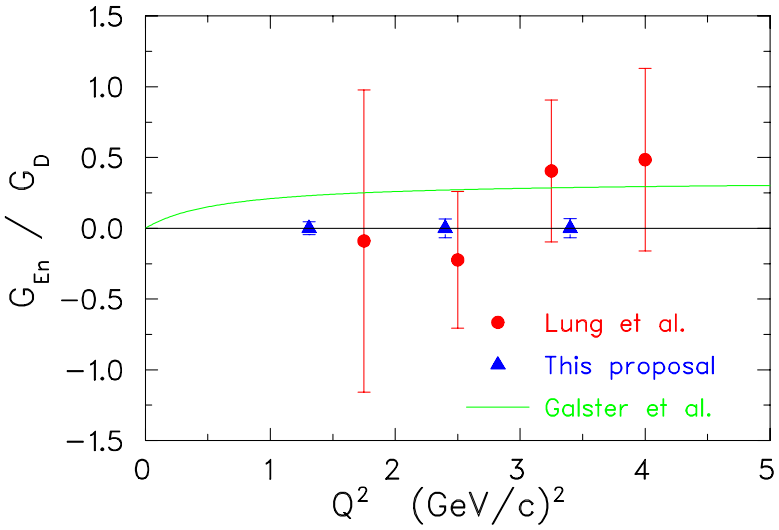

Figure 1: The ratio of the electric form factor of the neutron and the dipole form factor as function of Q^2 determined in quasi elastic $e-d$ scattering [6]. The solid line represents the prediction for G_{En} according to the Galster approximation [7], a phenomenological fit to low Q^2 data. The triangles show the projected data points of this proposal.

$-\mu_n\tau/(1+5.6*\tau)\cdot G_D$, where G_D is the dipole form factor and $\tau = Q^2/4m_N^2$.

Double polarization experiments provide another tool to study G_{En}. By investigating spin observables, the interference between G_{En} and G_{Mn} enhances the sensitivity of these reactions to G_{En}. This possibility was already discussed in 1969 by Dombey [8], and later by Akhiezer and Rekalo [9]. Arnold, Carlson, and Gross suggested studying the reaction $d(\vec{e},e'\vec{n})p$ to determine G_{En} [10]. In 1984 Woloshyn proposed the use of a polarized ^{3}He target to measure G_{En} [11]. There have been several proposals at JLab making use of this idea: McKeown proposed to study polarized electron scattering from a polarized ^{3}He target with CLAS in Hall B to test models of the structure of ^{3}He as well as to use this target as a "polarized neutron" in the measurement of G_{En} [12]; Hersman also proposed to use a polarized ^{3}He target together with the CLAS detector to measure G_{En} [13]; while in Hall A McKeown and Korsch proposed a measurement of G_{En} using a polarized ^{3}He target together with the HRS [14].

In the last ten years, a variety of double polarization experiments to measure G_{En} have been performed at different facilities: MIT-Bates, NIKHEF, MAMI, and JLAB Hall C. Figure 2 shows the published results on G_{En} obtained from these types of experiments [15, 16, 17, 18, 19, 20, 21, 22, 23, 24, 25]. Not shown are projected data points or preliminary results from JLab experiments E93-026 and E93-038 [26, 27]. Both experiments have already been run in Hall C, but the final results are not yet published. Both Hall C experiments, as well as the experiments at other facilities, are focused on lower momentum transfers, as compared to the proposed measurements of this proposal: the maximum momentum transfer of E93-038 is Q^2= 1.47 (GeV/c)^2, while E93-026 will stop at Q^2= 1.0 (GeV/c)^2.

In Fig. 1 the projected data points from the proposed experiment are shown, compared to the results from [6] and the empirical fit from [7]. To address the actual physics interests, we

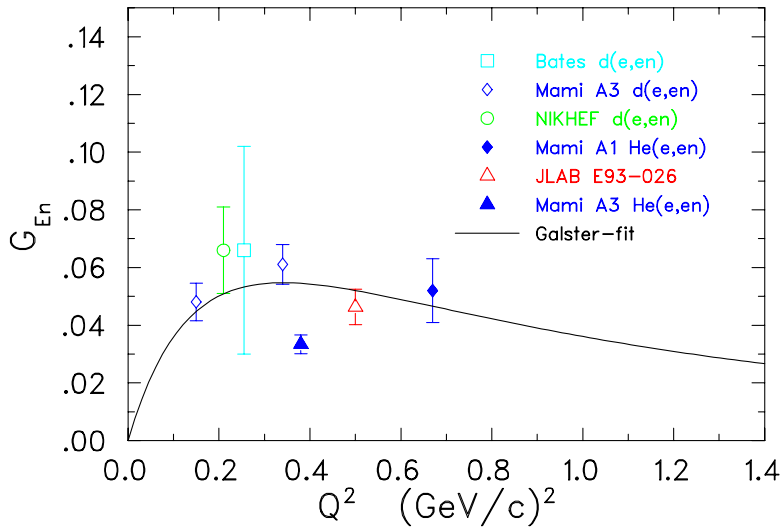

Figure 2: The published world data on G_{En} obtained from double polarization electron scattering experiments [15, 16, 17, 18, 19, 20, 21, 22, 23, 24, 25]. Further data from currently running Hall C experiments 93-026 and 93-038 [26, 27], which will cover Q^2 values of 0.43, 0.5, 1.0, 1.13, and 1.47 $(GeV/c)^2$, are not included.

propose to measure this quantity at Q^2=2.4, and 3.4 $(GeV/c)^2$. To study model dependencies originating from the use of a polarized ^{3}He target and to facilitate the comparison with experimental data obtained by other double polarization experiments, we additionally request to measure G_{En} at Q^2=1.3 $(GeV/c)^2$, which can be done without a significant increase in the beamtime request. We expect to achieve a statistical uncertainty in $\Delta G_{En}/G_{En}$ of 0.14 in each of the three data points in 768 hours of beamtime. This accuracy is comparable to the precision of the data on the proton, so a direct comparison of G_{En} and G_{Ep} will be possible. In this error estimate, we assumed that G_{En} follows the Galster parameterization. At this time, there is no accurate data available from double polarization measurements for Q^2 greater than 1.5 $(GeV/c)^2$. There is also no other approved experiment at JLab, which is the only laboratory where a double polarization measurement of G_{En} at such high momentum transfers is possible. JLab proposal 01-106 for PAC 20, which was deferred, proposed to measure G_{En} at Q^2= 2.4 $(GeV/c)^2$ [28]. This is the same Q^2 value as the second data point of this proposed measurement, but still much lower than our third data point. We will get all three measurements in a comparable time (768 hours). This is mainly due to two advantages: firstly, the large acceptance BigBite spectrometer and a neutron detector with an angular acceptance matched to the electron arm results in a large solid angle which cannot be achieved with any of the other standard detectors in Hall A or Hall C; second is the large degree of neutron polarization in the Hall A polarized ^{3}He target, which has a luminosity capability which exceeds that of other polarized targets. The use of the polarized ^{3}He target together with the polarized electron beam allows us to perform a double polarization experiment without the need to use a polarimeter to measure the polarization of the recoiling neutron. Additionally, due to the high momentum of the recoiling neutron, the neutron detector can be built with a very high neutron detection efficiency.

2 Physics Motivation

The nucleon plays the same central role in hadronic physics that the hydrogen atom does in atomic physics and the deuteron in the physics of nuclei. The structure of the nucleon and its general properties such as charge, magnetic moment, size and mass (and the appropriate form factors) are of fundamental scientific interest. The nucleon is a laboratory for the study of the quark-gluon interaction. Both nucleons, the proton and the neutron, need to be explored. At present the proton has been more thoroughly studied than the neutron. More data on the neutron is essential if we are to make real progress in obtaining a complete description of the quark structure of the nucleon.

Considerable information on the structure of the nucleon has been obtained by using electromagnetic probes via electron scattering. Inclusive deep inelastic scattering (DIS) has been a classical tool with which the partonic structure of the nucleon has been probed. At high Q^2, DIS yields information on the (light-cone) momentum space distributions of quarks and gluons in the nucleon (when viewed through the infinite momentum frame). Many of the experimental foundations of QCD are in fact derived from investigations of various aspects of DIS.

Exclusive processes, on the other hand, such as elastic electron and photon scattering, can provide information on the spatial distribution of the nucleon's constituents, which is parameterized through the elastic nucleon form factors. For photon scattering, only one set of data, obtained at Cornell in 1977 [29], on high energy scattering off the proton at large s, t, and u is available. Experimental studies of elastic electron scattering from both the proton and the neutron were initiated at SLAC and are now being thoroughly performed at Jefferson Lab.

The Dirac form factor F_1 describes the distribution of electric charge and the Dirac magnetic moment, while the helicity non-conserving Pauli form factor, F_2, describes the distribution of the Pauli magnetic moment; these two form factors are the key ingredients of the hadronic current. The Sachs form factors, G_E and G_M, the ratio of which will be extracted directly from our data, are related to F_1 and F_2 by:

$$F_1 = \frac{G_E + \tau G_M}{1+\tau} \text{ and } F_2 = \frac{G_M - G_E}{\kappa(1+\tau)}, \tag{1}$$

where $\tau = Q^2/4m_N^2$ and κ is the nucleon anomalous magnetic moment. The independent determination of G_{Mp} and G_{Ep} from the unpolarized ep cross section data has been made up to $Q^2 = 8.8$ (GeV/c)^2 [30]. The extraction of G_{Mp} from a single cross section measurement to higher Q^2 assumes $\mu_p G_{Ep}$=G_{Mp} [31]; these data are shown in Fig. 3.

In the case of the neutron, new measurements of G_{Mn} in Hall B [32] are currently being analyzed; they will bring the knowledge of this form factor to comparable levels of accuracy (at least 5%) up to $Q^2 = 4.8$ (GeV/c)^2. For the neutron electric form factor, two new JLab experiments, E93-026 [26] and E93-038 [27], will extend the Q^2 range to 1.5 (GeV/c)^2.

The PAC15 Workshop on Nucleon and Meson Form Factors and Sum Rules addressed the following scientific questions:

- What is the role of perturbative QCD in understanding nucleon form factors at high Q^2?

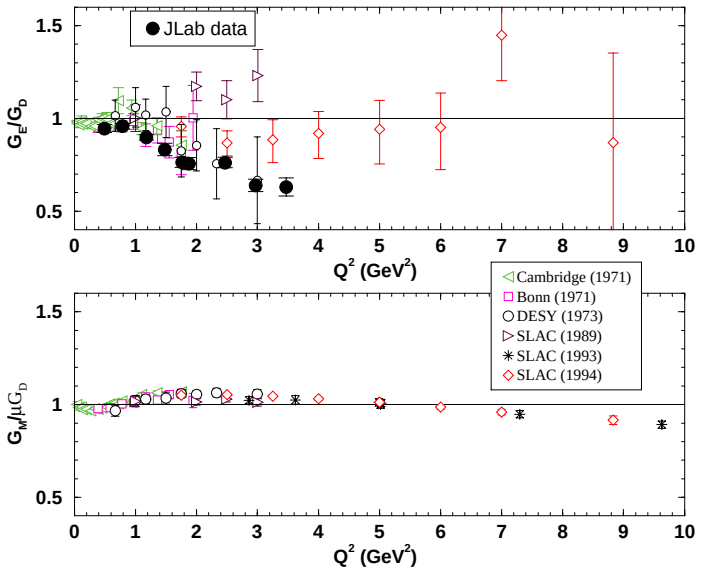

Figure 3: World data for G_{Ep}/G_D and for $G_{Mp}/\mu G_D$.

- Can we understand the nucleon as a strongly interacting few-body system?
- Can form factor ratios be calculated in believable QCD-motivated models?
- Can non-forward distributions provide a link between form factors and structure functions?

As we discuss in the following, the measurement of G_{En} at a few $(\mathrm{GeV/c})^2$ proposed here will provide fundamental information needed for answering these questions.

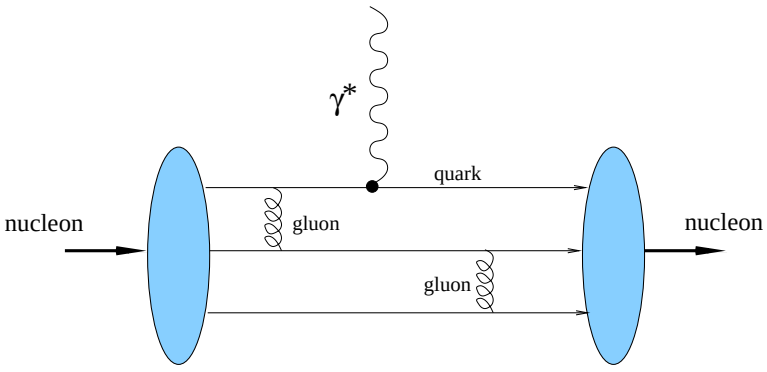

Figure 4: Two gluon exchange pQCD diagram.

At asymptotically high Q^2, one can apply perturbative QCD (pQCD) to describe the Q^2 dependence of exclusive electron scattering [33, 34]. The crucial question is where the perturbative, two-gluon exchange process (Fig. 4) makes the dominant contribution. Standard

pQCD analysis suggests that the F_1 form factors has a Q^{-4} dependence while F_2 has a Q^{-6} dependence; hence pQCD predicts that Q^2F_2/F_1 should become constant at high Q^2, as suggested by Brodsky and Farrar [33] and later discussed in detail by Brodsky and Lepage [34]. The onset of scaling in DIS at $Q^2 \sim$ 1–2 (GeV/c)^2 gave rise to expectations that pQCD might also be applicable to exclusive processes in the range of a few (GeV/c)^2. The recent JLab experiments E93-027 and E99-007 showed clear evidence, however, of soft regime dominance in the several (GeV/c)^2 range. In particular, the Q^2 dependence of G_{Ep} and G_{Mp} was found to be different, suggesting that their soft contributions are different [2, 3]. Presently the theoretical expectation for the transition to the pQCD regime is at much higher Q^2, perhaps of the order of 10's of (GeV/c)^2.

Over the years many QCD-inspired models have been developed to describe nucleon electromagnetic form factors at small and intermediate Q^2 values ($Q^2 \leq$ 1–2 (GeV/c)^2). While these have provided some insights into the possible origin of the nonperturbative quark structure of the nucleon, ultimately one would like to use experimental form factor data to test the working of QCD itself. During the last few years an important development in QCD phenomenology has been the exploration of the generalized parton distribution (GPD) formalism [35, 36, 37], which provides model–independent relations between inclusive and exclusive observables. For example, the nucleon elastic form factors F_1 and F_2 are given by the first moments of the GPDs [36]:

$$F_1(t) = \sum_q \int_0^1 F_\zeta^q(x,t)dx \;\; \text{and} \;\; F_2(t) = \sum_q \int_0^1 K_\zeta^q(x,t)dx, \tag{2}$$

where F_ζ^q and K_ζ^q are the non-forward generalizations of the Dirac and Pauli form factors, respectively [36]. In 1998 Radyushkin demonstrated the dominance of the handbag diagram (Fig. 5) for moderate momentum transfers, Q^2 in the range of 10 (GeV/c)^2, and examined links between different exclusive processes, such as elastic electron scattering, Compton scattering and DIS [38]. Subsequently Diehl et al. [39, 40] analyzed the effects of higher Fock states and calculated various polarization observables. These calculations [38, 39, 40] provide a framework for constraining GPDs via measurements of the nucleon form factors. In particular, since at large Q^2 ($= -t$) the magnetic form factor is dominated by the Dirac form factor, $F_1(t)$, data on the G_E form factor will be crucial in providing constraints on the spin-flip GPD, K_ζ^q, through the Pauli form factor, $F_2(t)$. Accurate data on G_{En} at several (GeV/c)^2 will therefore open additional dimensions for testing the GPD approach.

The isovector and isoscalar form factors constructed from the proton and neutron form factors have different sensitivity to higher Fock components of the light cone quark wave function. This difference can be an important handle to test the valence quark dominance in exclusive reactions in the few (GeV/c)^2 range. Data on F_{1p} and F_{1n} will allow the extraction of information related to the *(u-d)* distribution, which was calculated recently using the GPD approach by K. Goeke, M. Polyakov, and M. Vanderhaeghen [41].

Recent theoretical developments also indicate that measurements of the individual elastic form factors of the nucleon up to high Q^2 may shed light on the problem of nucleon spin [42]. Furthermore, as shown earlier by Ji [35], the second moment of the GPD corresponding to the function F_ζ^q taken in the forward limit yields, according to the Angular Momentum

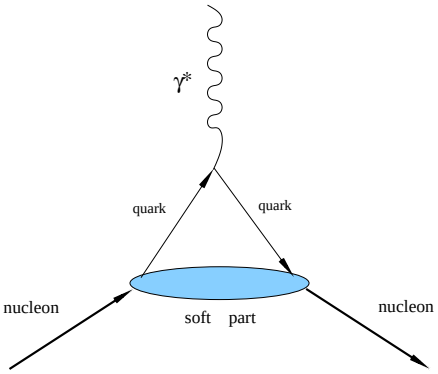

Figure 5: The handbag diagram for elastic electron–nucleon scattering.

Sum Rule, the contribution to the nucleon spin from quarks and gluons, including both the quark spin and orbital angular momentum.

As an incidental benefit of the proposed experiment, a better determination of the neutron electric form factor will be very important for calculations of nuclear form factors, such as those of the deuteron. Even though $G_{En} \ll G_{Ep}$ at $Q^2 \approx 0$, at larger Q^2 ($Q^2 \sim 3$ (GeV/c)^2) the ratio G_{En}/G_{Ep} can be as large as $\approx 40\%$, so that accurate information on G_{En} at large Q^2 is essential for a reliable description of the deuteron form factors.

Finally, we should also point out that there is a major effort underway by the Lattice Hadron Physics Collaboration, led by Jefferson Lab and MIT, to calculate elastic form factors of the nucleon using lattice QCD. At present only exploratory calculations of G_{En}, mostly at low Q^2, have been performed [43], and the proposed lattice simulations will use new techniques and greater computing resources to compute G_{En} over a large range of Q^2, both in the quenched approximation and with dynamical sea quark effects [44].

3 The Double Polarization Method

In the following paragraphs we will briefly summarize the formalism used to describe cross sections and asymmetries obtained in doubly polarized electron scattering experiments. We will mainly follow the approach of [45, 46]. In the Born approximation, the elastic electron nucleon scattering $(e-N)$ cross section can be written as a sum of two parts: Σ, which corresponds to the unpolarized elastic cross section $d\sigma/d\Omega_e$, and a polarized part Δ, which is only non-zero if the electron is longitudinally polarized (helicity $h = \pm 1$)

$$\sigma_h = \Sigma + h\Delta. \tag{3}$$

The asymmetry A_N for the $e-N$ scattering cross section is defined as

$$A_N = \frac{\sigma_+ - \sigma_-}{\sigma_+ + \sigma_-} = \frac{\Delta}{\Sigma}. \tag{4}$$

The unpolarized $e-N$ cross section Σ for elastic scattering off a free nucleon at rest is given – again in the Born approximation – by

$$\Sigma = \sigma_M \left(\frac{G_E^2 + \tau G_M^2}{1+\tau} + 2\tau G_M^2 \tan^2(\theta/2) \right), \tag{5}$$

with

$$\sigma_M = 4\alpha^2(\hbar c)^2 \frac{E_f^2}{Q^4} \cos^2(\theta/2) \frac{E_f}{E_i} \tag{6}$$

being the Mott cross section, which describes the scattering from a pointlike target. In the above equations, E_i (E_f) is the electron's initial (final) energy, m_N the mass of the nucleon, Q^2 the (negative) square of the four–momentum transfer, and G_E (G_M) the electric (magnetic) Sachs form factor of the nucleon. The polarized part is given by

$$\Delta = -2\sigma_M \sqrt{\frac{\tau}{1+\tau}} \tan(\theta/2) \left[\sqrt{\tau(1+(1+\tau)\tan^2(\theta/2))} cos\theta^\star G_M^2 + \sin\theta^\star \cos\phi^\star G_M G_E \right], \tag{7}$$

where $\theta^\star$ is the polar angle and $\phi^\star$ is the azimuthal angle of the target polarization in the laboratory frame with respect to the axis of the momentum transfer (see Fig. 6).

The measured experimental asymmetry for the $^3\vec{H}e(\vec{e}, e'n)$ reaction is reduced compared to this ideal $\vec{n}(\vec{e}, e'n)$ reaction because of the finite polarization of the electron beam P_e, the finite polarization of the neutrons P_n in the ^3He target, the dilution D of atoms other than ^3He in the target, and the dilution $V = (1 + N/S)^{-1}$ of events originating from random coincidences and reactions other than quasi-elastic scattering, where N/S is the noise–to–signal ratio. At JLab beam polarizations of $P_e = 0.75$ are routinely achieved. The polarized $^3\vec{H}e$–target has been operated at average values of $P_{He} = 0.40$ during experiments E99-117 and E97-103. The total spin of ^3He is mainly carried by the neutron, so a polarized ^3He target represents an effective polarized neutron target. As many authors have shown [47, 48, 49, 50, 51, 52, 53], even for a 100% polarized ^3He nucleus the neutron itself has only a polarization of 0.86 ± 0.02. Additionally, the protons are not completely unpolarized, but

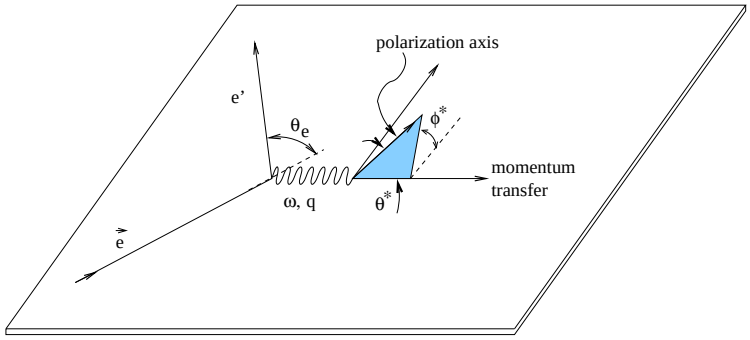

Figure 6: The kinematics of electron scattering from a polarized target.

have a polarization of 0.028 ± 0.004. So the polarization of the neutron P_n is only 86% of the polarization of ^3He. Lastly, the presence of nitrogen in the target cell leads to $D = 0.94$ and background events lead to $V = 0.91$ (see Sec. 4.3 and 6).

The measured asymmetry from the neutron can now be expressed as follows:

$$A_{exp} = P_e \cdot P_n \cdot D \cdot V \cdot A_{phys} \tag{8}$$

with

$$\begin{aligned} A_{phys} = \; & - \; \frac{2\sqrt{\tau(\tau+1)}\tan(\theta/2) G_{En} G_{Mn} \sin\theta^\star \cos\phi^\star}{(G_{En})^2 + (G_{Mn})^2(\tau + 2\tau(1+\tau)\tan^2(\theta/2))} \\ & - \; \frac{2\tau\sqrt{1+\tau+(1+\tau)^2\tan^2(\theta/2)}\tan(\theta/2)(G_{Mn})^2\cos\theta^\star}{(G_{En})^2 + (G_{Mn})^2(\tau + 2\tau(1+\tau)\tan^2(\theta/2))} \; . \end{aligned} \tag{9}$$

By aligning the target spin perpendicular to the momentum transfer, one gets the perpendicular asymmetry:

$$A_{perp} = -\frac{G_{En}}{G_{Mn}} \cdot \frac{2\sqrt{\tau(\tau+1)}\tan(\theta/2)}{\left(G_{En}/G_{Mn}\right)^2 + (\tau + 2\tau(1+\tau)\tan^2(\theta/2))} \; . \tag{10}$$

Because $(G_{En}/G_{Mn})^2$ is small compared to the second term of the denominator in our kinematics, G_{En} is nearly proportional to A_{perp}. To extract G_{En} out of this ratio, knowledge of G_{Mn} is necessary. Fortunately, G_{Mn} is sufficiently well known. Experiment E94-017 in Hall B recently did a measurement of G_{Mn} up to $Q^2 = 4.8$ (GeV/c)^2 which will provide very accurate data [32]. Due to the large acceptance of the BigBite spectrometer and the neutron detector array, the perpendicular spin alignment can only be made for part of the acceptance, and longitudinal contributions to the asymmetry have to be taken into account:

$$A_{long} = -\frac{2\tau\sqrt{1+\tau+(1+\tau)^2\tan^2(\theta/2)}\tan(\theta/2)}{(G_{En}/G_{Mn})^2 + (\tau + 2\tau(1+\tau)\tan^2(\theta/2))} \tag{11}$$

Nevertheless these contributions are small, and depend – to first order – only on the kinematics, not on the value of G_{En} itself. Together with the ability to reconstruct the scattering

angles and the momentum transfer, these corrections are under control. A more detailed discussion follows in Sec. 6.5.

The above discussion described scattering from a free nucleon. The general case of electron scattering from a bound nucleon was also analyzed by Donnelly [46]. Additional components, which appear in the cross section, are nulled when the cross section is integrated over the azimuthal angle of the nucleon momentum relative to the direction of the momentum transfer and the electron scattering plane. The Fermi motion of the nucleon inside the nucleus leads to kinematical effects on A_{perp}. Because of the dependence of the $\gamma^{\star}n$ cross section on the internal momentum of the nucleon the average energy of the scattering is reduced as compared to the free nucleon at rest. As a result a nonzero value of A_{long} appears. The remaining differences between the case of a free and a bound nucleon will be addressed in Sec. 5.

4 Experimental Setup

As illustrated in Fig. 7, this experiment will study the scattering of polarized electrons from polarized ^{3}He. The scattered electron will be detected in the BigBite spectrometer, while a new, large solid angle scintillator array, matched to the BigBite acceptance, will be used to detect the recoiling neutron. The polarized target geometry will be slightly modified if necessary to ensure compatibility with BigBite. We will also make use of enhanced target cells to ensure optimal performance during the experiment. The BigBite spectrometer is scheduled to have its trigger plane upgraded in 2002 by the BigBite collaboration [54]. We will use this upgraded configuration. The neutron detector will be constructed by this collaboration. It will use existing and new neutron bars from several of the collaborating institutions. The following subsections describe in more detail the modifications and additions necessary to carry out this experiment.

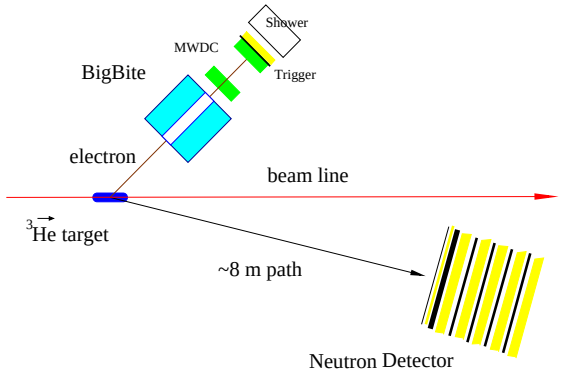

Figure 7: Layout of the experimental setup.

4.1 The CEBAF Polarized Beam

In our rate calculations we have assumed 12μA of beam with 75% polarization. Currents in excess of 12μA with beam polarization as high as 75% have already been delivered over long periods of time using the strained GaAs source at Jefferson lab. The beam polarization will mainly be measured with the Hall A Møller polarimeter, which is able to measure this quantity with a systematic uncertainty of 3%. This uncertainty can be improved by calibrating the Møller polarimeter against the Compton polarimeter, which itself has only a systematic uncertainty of 1.4%, but cannot be used directly to measure the beam polarization because of the low beam current of 12 μA.

4.2 The Polarized ^{3}He Target

The experiment will utilize the polarized ^{3}He target that has been constructed and successfully employed for a series of experiments in Hall A. First installed in 1998, the Hall A polarized ^{3}He target was constructed through a collaborative effort between JLab and several participating institutions. It was first used for E94-010 and E95-001. Quite successful in its first run, the polarized ^{3}He target was further improved prior to being installed for a second set of experiments including E99-117 and E97-103 in 2001. We anticipate that this refinement process will continue, making our projections for target characteristics, which are based on demonstrated performance, quite conservative.

4.2.1 The Principles of the Polarized ^{3}He Target

The target is based on the technique of spin-exchange optical pumping which can be viewed as a two step process. In the first step, an alkali-metal vapor such as rubidium (Rb) is polarized by optical pumping using radiation from a laser. In the second step, the polarized Rb atoms collide with ^{3}He atoms, transferring their spin to the ^{3}He nuclei through the hyperfine interaction. Both the Rb atoms and the ^{3}He are contained in sealed glass cells.

The time-dependent polarization of the ^{3}He can be described by:

$$P_{\rm He}(t) = P_{\rm Rb}\,\frac{\gamma_{se}}{\gamma_{se}+\Gamma}\left(1-e^{-t(\gamma_{se}+\Gamma)}\right) \tag{12}$$

where $P_{\rm He}$ is the nuclear polarization of the ^{3}He, $P_{\rm Rb}$ is the polarization of the Rb, γ_{se} is the rate of spin-exchange between the ^{3}He and the Rb, and Γ is the spin-relaxation rate of the ^{3}He nuclei due to all other processes. Spin exchange between Rb and ^{3}He is quite slow, with $1/\gamma_{se}$ being on the order of 12 hours. From equation 12, it can be seen that in order to achieve high polarizations, we must have the relaxation rate $\Gamma << \gamma_{se}$. Some of the contributions to Γ are intrinsic to the various target cells. These intrinsic contributions include relaxation due to ^{3}He–^{3}He collisions, and relaxation due to ^{3}He–wall collisions. Calling the intrinsic component to the relaxation Γ_{cell}, it is desirable to have cells in which Γ_{cell}^{-1}, which we often refer to as the cell lifetime, is $40-60$ hours. Producing a collection of target cells with such long lifetimes is an important component of preparing the polarized ^{3}He target for an experiment.

4.2.2 Components of Hall A Polarized ^{3}He Target

At the heart of the target system are sealed glass "target cells", pictured toward the center of Fig. 8, each of which contains approximately 10 atmospheres of ^{3}He, around 70 Torr of nitrogen, and a few droplets of Rb metal. The cells have two chambers: an upper "pumping chamber" in which the optical pumping and spin exchange take place, and a lower "target chamber" through which the electron beam passes during the experiment. The chambers are connected by a transfer tube that allows the ^{3}He to diffuse back and forth between the two chambers with a time scale that is short compared to the time it takes (roughly 24–48 hours) to polarize a cell.

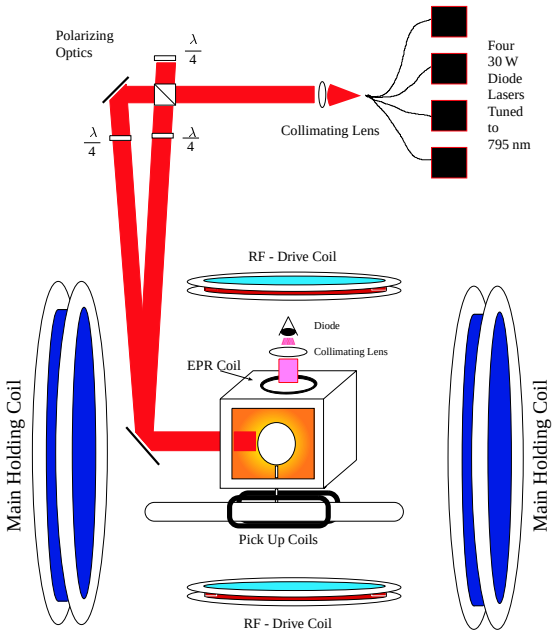

Figure 8: Schematic of the Hall A polarized ^{3}He target. Shown are the optics and target cell, the RF coils and one set of Helmholtz coils.

The magnetic holding field is roughly 25 Gauss, and is supplied by two large sets of coils that are roughly in Helmholtz configuration. There is some concern that the coils will physically interfere with the close placement of Bigbite. If this is the case, somewhat smaller coils can be used. For instance, the smaller of the two sets of coils can be kept, and a second even smaller set can be constructed. Since the coils are of a simple air-core variety, the lead time would not be long should this be necessary. This decision will be made as the design details of Bigbite become available.

Polarimetry is provided by two separate systems. One system is based on the NMR technique of adiabatic fast passage (AFP). During an AFP measurement, an rf field is applied to the target while the magnetic holding field is swept through the resonance condition. The resulting signal is detected by "pick-up coils". This system is calibrated by comparing the signal size with the AFP signal from a water sample, the thermal polarization of which is well understood. The second form of polarimetry is based on electron paramagnetic resonance (EPR). The EPR frequency of the Rb is measured using an optical detection scheme, and a small shift is observed due to the presence of the polarized ^{3}He. The size of the shift, which is proportional to the ^{3}He polarization, can be determined in a manner that is quite free of systematics by reversing the polarization of the ^{3}He with respect to the applied magnetic field. The use of two independent forms of polarimetry increases our confidence that the polarization of the target is well understood.

4.2.3 Preparation and Improvements for Measuring G_{En}

Several important steps will be undertaken to ensure optimal performance of the Hall A polarized target during the experiment.

Firstly, multiple target cells will be constructed prior to the experiment and they will be carefully characterized in order to select only those cells that yield optimal performance. This strategy was employed during E99-117 and E97-103 in 2001, and resulted in the best performance to date of a polarized ^{3}He target in an accelerator based experiment. Targets were tested for their intrinsic lifetime, and also for the maximum polarization that they achieved. Only those targets performing well in both tests were selected.

Another important step we are pursuing involves fundamental improvements to the target cells. The best polarizations that have been measured in JLab-style targets are on the order of 45–50%. Using equation 12, however, together with established spin-exchange parameters and the measured properties of the cells, higher polarizations than those observed are expected. Several possibilities exist that would explain the suppressed polarization, including the evolution of impurities from the glass during operating conditions. To address this possibility, we have developed a coating technique based on sol-gel technology, in which the interior surface of the cell is coated with a layer of glass that is pure and free of impurities. Tests of this technique will be complete well before the running of our experiment, and should improvements be observed, we will incorporate the new cell designs into our experiment. Our hope is that higher polarizations can be achieved, or at the very least, a greater success rate can be demonstrated for the fabrication of target cells with good performance characteristics.

Finally, as the final design details of Bigbite are established, we plan to ensure that good compatibility exists with the polarized target. Of particular concern are magnetic field gradients from the Bigbite magnet. We plan to supress them as much as possible using a field clamp (see Sec. 4.3.4). The impact of any residual inhomogeneities can be checked during bench tests prior to the installation of the target. It is anticipated that residual inhomogeneities will not be a problem for the normal operating configuration of the target, but may be a limiting factor during polarization measurements. If this is the case, one easy solution would be to turn Bigbite off during measurements. Another would be to employ the use of shim coils.

4.3 BigBite Spectrometer

Scattered electrons will be detected in the BigBite spectrometer (Fig. 9). BigBite is a non-focusing large momentum and angular acceptance spectrometer that was originally designed and built for use at the internal target facility of the AmPS ring at NIKHEF [55, 56]. The spectrometer consists of a single dipole magnet (maximum magnetic field 1.2 Tesla) and a detection system. The original detector package included two sets of multi-wire drift chambers (MWDC), a plastic scintillator and an aerogel Cerenkov detector. To cope with the high rates possible at JLab, it was decided to upgrade the detector package (Fig. 10). This upgrade is needed for several experiments in Hall A, including E01-014 and E01-015. The single large scintillator will be replaced by a segmented two-layer array of plastic scintillators, with the first ΔE layer consisting of thin (3 mm) counters and the second E layer consisting of 3 cm thick counters. Each plane will be segmented into 24 elements which will be read out on both sides by fast PMTs. There are also plans to replace the original MWDC with MWPC to improve the rate capability. However, we wish to employ the MWDC for this experiment because of their higher resolution (*cf.* Fig. 11). The momenta of the scattered electrons in this experiment will be between 1200-1500 MeV/c. In order to make their field integral through the BigBite dipole as large as possible, the magnet will be run at its maximum field of 1.2 T. To minimize field gradients at the position of the polarized Helium target, a field clamp will be added to the spectrometer.

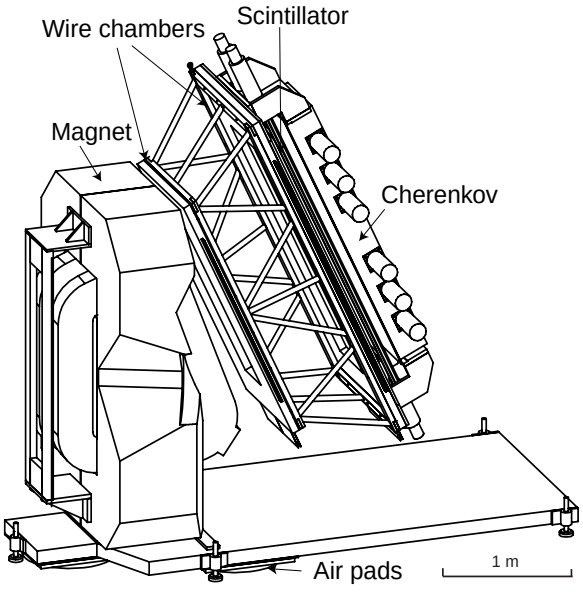

Figure 9: An overview of the BigBite spectrometer. Shown (from left to right) are the bending magnet (B_{max}=1.2 T), two MWDC, the scintillator plane and the aerogel Cerenkov detector. This is the original detector stack configuration.

In order for us to accurately determine the scattered electron's angular coordinates, momentum and the position of the scattering vertex along the target, the optics of BigBite need to be studied. Coincidence elastic scattering will be used to calibrate the optics. The beam

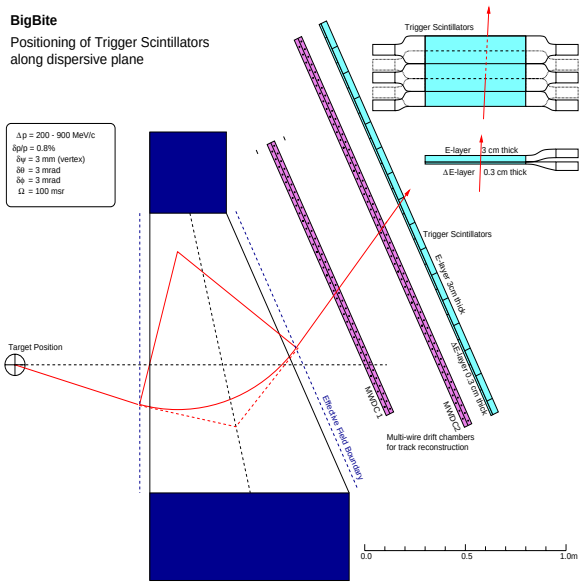

Figure 10: The BigBite spectrometer with modified detector stack.

will be scattered off a thin CH_2 target. BigBite will be centered at 54° in order to detect elastically scattered electrons, while protons scattered at 29° will be detected in the neutron detector scintillator array. The advantage of this method is the calibration location is the same as the proposed experimental Q^2=2.4 $(GeV/c)^2$ point. Therefore, systematic errors related to moving BigBite are avoided. The large out-of-plane acceptance of BigBite is, by design, well matched to the neutron detector out-of-plane acceptance.

A multi-foil carbon target will be used to calibrate the y_{target} reconstruction of the BigBite spectrometer. The calibration will be performed at first with the B field set to zero, which will offer a check of the wire chamber geometry. The B field will then be turned on to its full value for the optics calibration. These techniques are similar to those that were developed at NIKHEF to originally commission the BigBite spectrometer [55, 56].

4.3.1 Geant Simulation of BigBite

The package of programs for the simulation of the BigBite spectrometer characteristics was developed by V. Nelyubin [57]. In the proposed experiment the momentum of the scattered electron will exceed the original specs of BigBite. Results of a MC study of the BigBite momentum resolution for two different coordinate systems are shown in Fig. 11, where the momentum resolution as a function of the electron momentum for a position resolution of 0.2 mm (the resolution of the MWDC) and for a position resolution of 1.0 mm (the resolution of the MWPC) are plotted. For this experiment, the momentum of the scattered electrons will be between 1200-1500 MeV/c, leading to an expected momentum resolution of δp/p between 1.0-1.5%, assuming the MWDC are used. The expected position resolution on target along the beam is σ= 6 mm, and the expected angular resolution in both scattering planes is σ=1-1.5 mrad.

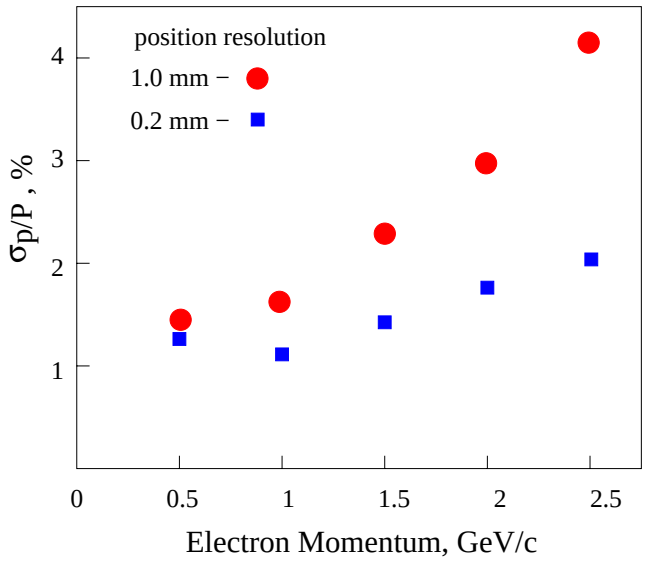

Figure 11: BigBite momentum resolution as function of the electron momentum for a position resolution of 0.2 mm (the resolution of the MWDC) and for a position resolution of 1.0 mm (the resolution of the MWPC). These are the results of a complete Monte Carlo study of the BigBite spectrometer at 50° using a gaseous helium target.

Additional MC studies were done to evaluate the parameters of the proposed experiment. Figure 12 shows a top and a side view of BigBite and the other experimental components as they were described in the simulations. The range of Q^2 accepted by the electron arm is shown in Fig. 13. The shaded area represents the events which will be used in the analysis of the highest Q^2 point ($\theta = 50^o \pm 4^o$). The same cuts on the angles and detector acceptance were used for the determination of the solid angle. The Q^2 resolution is on the order of 0.050 $(\mathrm{GeV/c})^2$, much smaller than the range of Q^2 itself. The resolution in W is 45 MeV, which is comfortably small compared to the proposed width of the W cuts of 200–400 MeV.

The solid angle of the electron arm for different positions along the target is shown in Fig. 14, where events were selected which had an electron momentum of 1.5 GeV/c and scattering angles of $50 \pm 4°$. The target length can be represented as 25 cm/sin(θ). The average solid angle is 76 msr.

The large angular acceptance of the electron arm leads to a considerable variation of the A_{long} component of the asymmetry. The MC simulations for A_{phys} with G_{En}=$G_{Galster}$ and G_{En}=0 are shown in Fig. 15.

4.3.2 BigBite Detector Stack

The particle tracking will be performed by the existing MWDCs with an upgraded DAQ. A 3 cm thick iron plate will be placed behind the second MWDC to protect the trigger planes from low-energy (less than 150 MeV) protons. The trigger will be formed by two segmented planes of scintillator counters. A lead glass shower detector will be placed behind the trigger

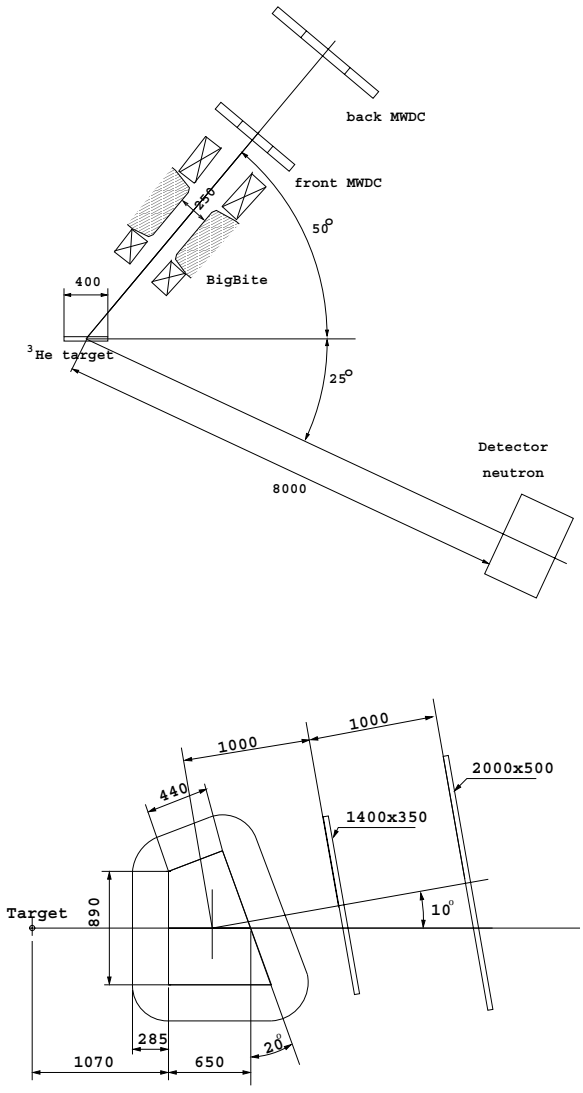

Figure 12: The top and side views of the experimental setup in the MC simulation. Dimensions are given in mm.

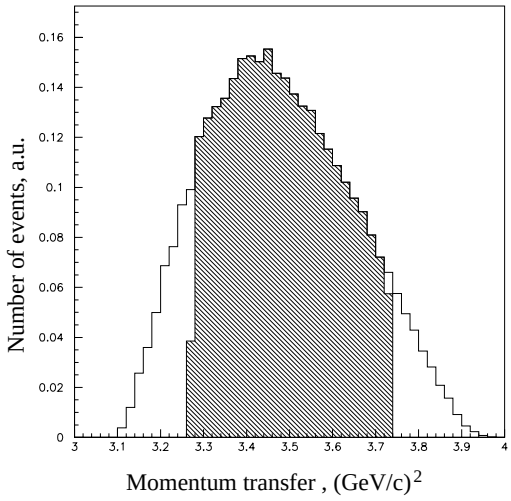

Figure 13: The momentum transfer range accepted in the BigBite spectrometer. The shaded area shows the events within a $\pm 4^o$ range of the central ray θ.

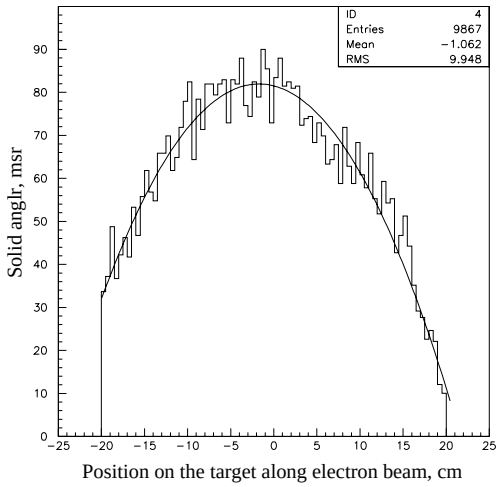

Figure 14: The MC simulation of the BigBite solid angle versus the position on target along the beam direction.

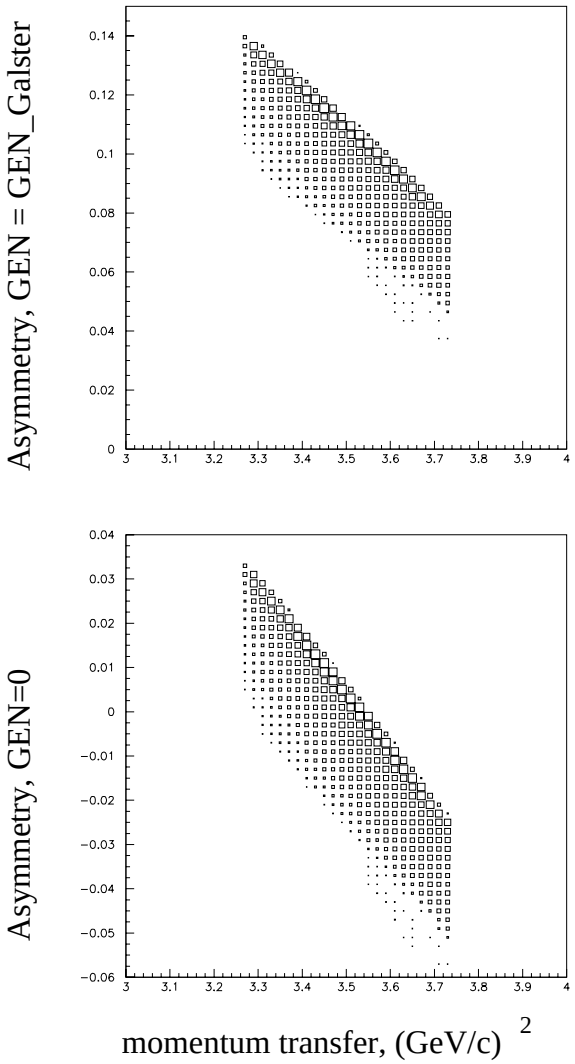

Figure 15: Event distribution as a function of the asymmetry A_{phys} and the momentum transfer. The upper plot is generated for G_{En}= $G_{Galster}$, the lower one for G_{En}=0.

planes. The shower counter will allow the measurement of the electron's energy with a 10% resolution, which is sufficient to suppress background from other particles. We plan to use the shower detector from the HRS-R which has an active area of 75x240 cm^2.

4.3.3 Background Rate in BigBite

A MC simulation [58] was used for the calculation of the rate on the MWDC and the trigger planes of the BigBite detector. Figure 16 shows the yield of protons for the conditions of our experiment at different energies and angles. Charged particles with momenta below 200 MeV/c will be deflected out of the acceptance by the BigBite dipole. The majority of background particles with momentum above 200 MeV/c are protons. Such protons have a rate of 3 MHz, which is uniformly distributed over the MWDC. The MWDC has 70 wires with an active area of 30 cm, so the expected rate is well below the rate limitation of the wire chamber. The maximum drift time in the MWDC is about 300 ns, so the average number of background hits per good event is about one. The true event hit in the second MWDC will be identified by using coordinate information from the segmented trigger. In addition, an analysis of the trajectory from the target to the MWDC will allow us to reduce the probability of a false hit in the front MWDC by a factor of 50.

The total expected rate on the trigger plane is 200 kHz, which is the combined rate from protons, pions and electrons. Off-line analysis of the shower detector, where electrons of interest deposit 1.2–1.5 GeV of energy, will reduce the background rate to 10 kHz of mainly high energy electrons.

4.3.4 The Field Clamp Configuration for Bigbite

The operation of the $^3\vec{H}e$ target requires small magnetic field gradients (the gradient averaged over the target volume must be below 30 mGauss/cm). The BigBite spectrometer was used at NIKHEF with an internal $^3\vec{H}e$ target [59]. It was found that the field clamp covering only the coils (see Fig. 9) was sufficient to keep the gradient below 30 mGauss/cm for dipole excitations up to 0.9 Tesla. Above this level the fringe field of the saturated iron yoke created larger gradients.

We plan to put a field clamp which will isolate the BigBite dipole from the target. Figure 17 shows the concept of the field clamp. The idea is to put an iron plate perpendicular to the magnetic holding field. An identical plate will be located on the opposite side to cancel first order distortions of the field induced by the first plate. The "red" coils provide most of the field. The "blue" coils are used to get good field uniformity. The "black" coils allow us to change the direction of the field by a few degrees without rotating the field clamps.

A complete 3–D calculation with the MAFIA package was performed for a configuration which includes the coils and the clamps from Fig. 17, but not BigBite. The field gradient was found to be below 20 mGauss/cm in the target volume even without using the blue coils. The blue coils allow a reduction of the gradient by an additional factor of 4.

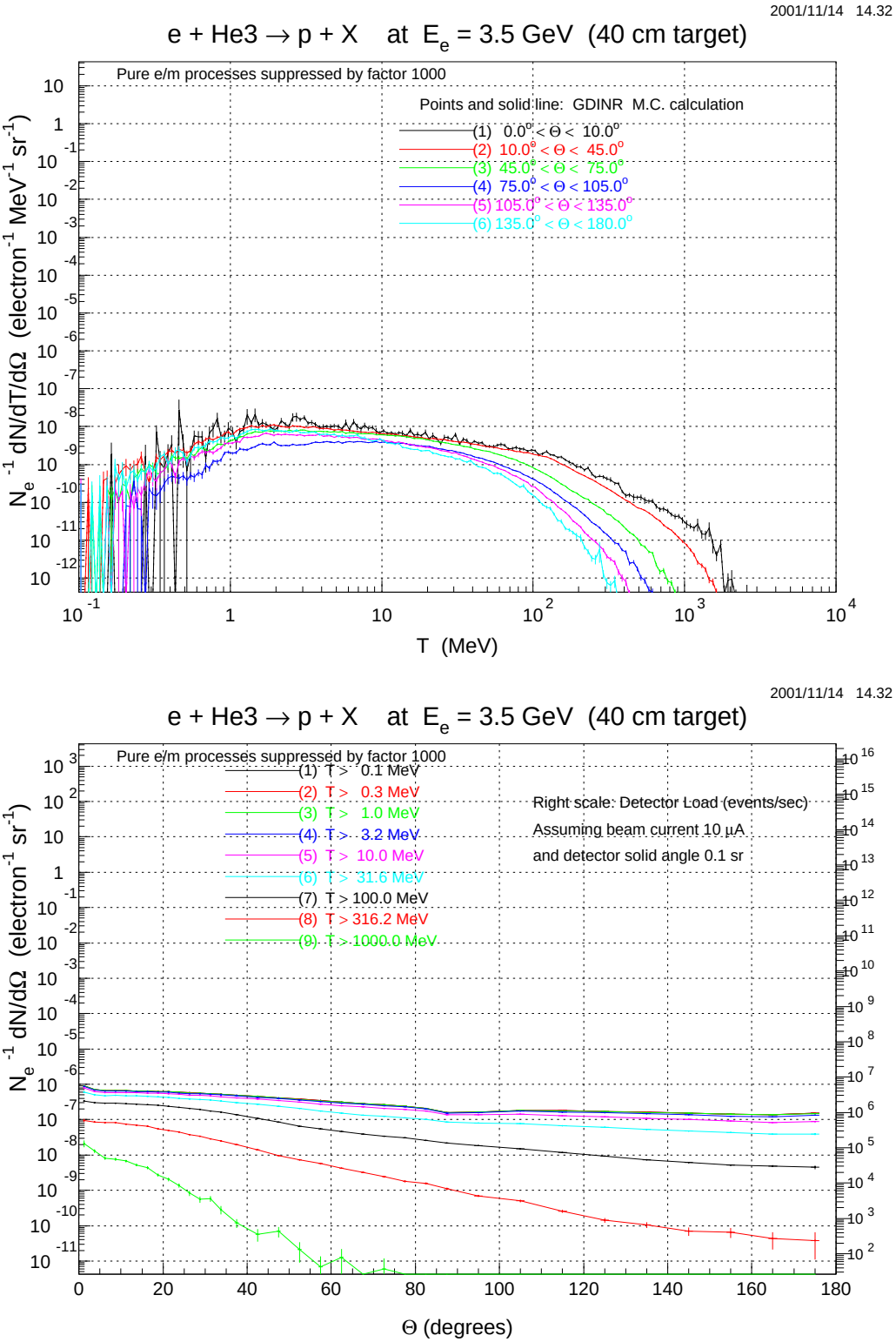

Figure 16: The proton yield with kinetic energy above given thresholds.

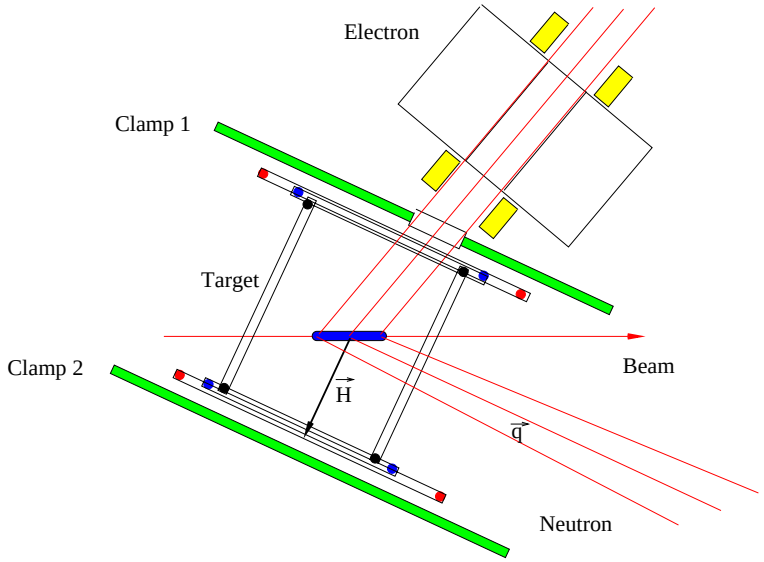

Figure 17: The concept of the field clamp configuration for the BigBite dipole.

4.4 Neutron Detector

The design of the neutron detector for this experiment is based on many considerations, including detector acceptance and efficiency, background suppression, and availability of the counters and electronics. There are several considerations which are specific to the conditions of the proposed experiment:

- The large kinetic energy of the neutron leads to the possibility of using high thresholds in the trigger and for off–line analysis.
- The relatively low luminosity for the polarized ^{3}He target simplifies the background situation.
- The high velocity of the neutrons demands the largest possible distance from the target.

The required acceptance of the neutron detector was evaluated in two steps. First we found from the MC the acceptance for exact elastic scattering (*cf.* Fig. 18). On the second step the size was increased in each direction to insure the acceptance of all events with a p_{mperp} of at least 150 MeV/c. For the $Q^2 = 3.4$ (GeV/c)^2 point, the horizontal and vertical size of the neutron detector must be increased by $\pm$ 47 cm in both directions. For the lower Q^2 points the distance between the target and the neutron detector will be shortened.

The structure of the detector is presented in the following section. It was optimized to have the best efficiency for a neutron momentum of 2.58 GeV/c and a threshold of 150 MeV. The trigger logic presented in the last section will allow us to use a high hardware threshold.

4.4.1 Structure of the Neutron Detector

This experiment is focused on large momentum transfer, where the recoiling neutrons have kinetic energies of 0.7 GeV, 1.3 GeV, and 1.8 GeV. Such large energies allow a high detection efficiency for neutrons, and at the same time they allow us to apply relatively high thresholds to suppress background from low energy particles. The proposed detector layout is presented in Fig. 19. The detector will have five layers, consisting of 40, 40, and 39 plastic neutron counters in the first, second, and third layer. Most of the counters in the front layers have dimensions 10x10x160 cm^3. In the fourth layer there are 20 counters. These counters have dimensions 10x20x180 cm^3. The fifth layer will be constructed from three types of detectors with different sizes: three counters are the same as those of the forth layer, 22 counters will have dimensions 10x25x100 cm^3 and 12 counters will have dimensions 10x10x100 cm^3. Each neutron bar is equipped with two photomultipliers, one on each end. In front of every layer there is a 2.75 cm iron converter to increase the probability of a neutron interaction in the detector. The front of the detector will be covered by a segmented veto detector protected by a 2 cm thick iron plate. Between the veto counters and the front layer of the neutron bars, there will be an additional 3.75 cm thick iron plate to provide additional shielding from low energy particles.

The performance of the proposed detector was evaluated by using GEANT-3 Monte Carlo simulations. The reliability of GEANT using Fluka neutron interactions with matter was analyzed recently in [60]. It was demonstrated that for neutrons with kinetic energy above 1 GeV, GEANT reproduces experimental results.

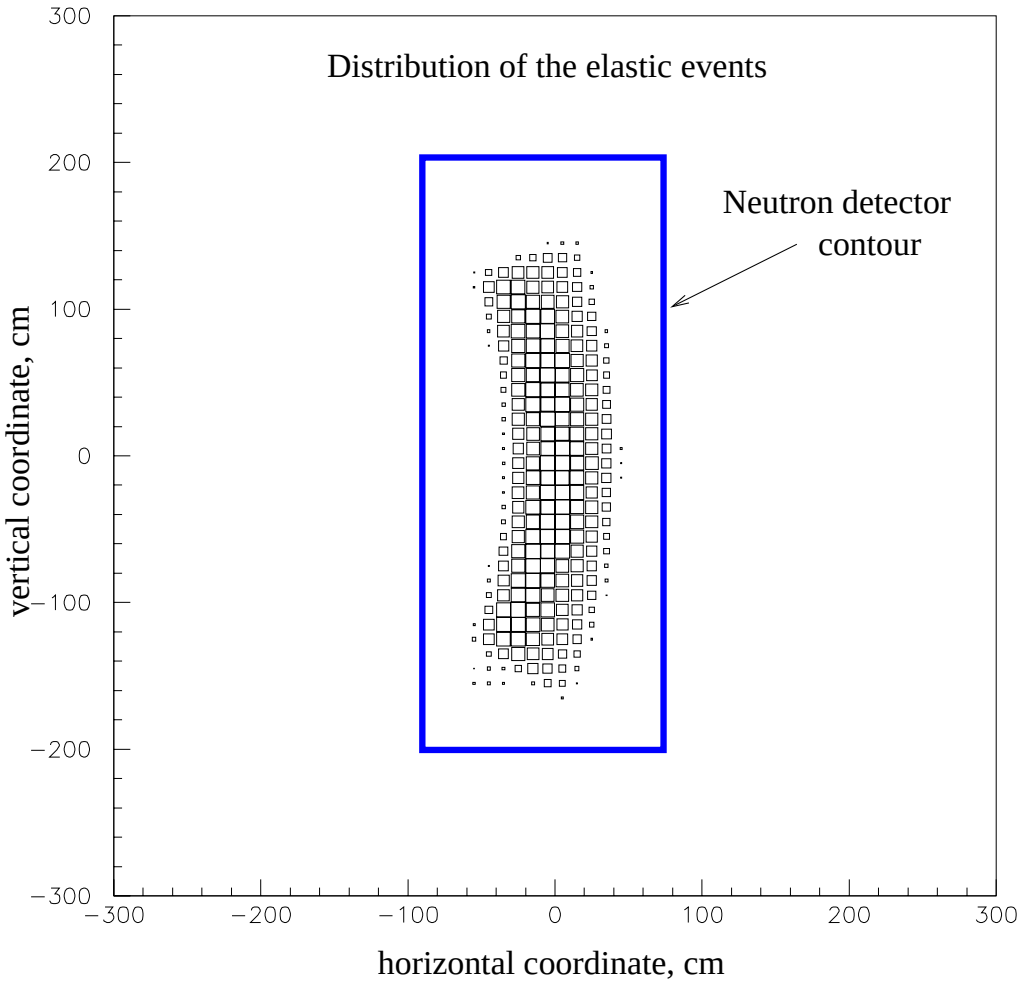

Figure 18: Required dimensions of the neutron detector.

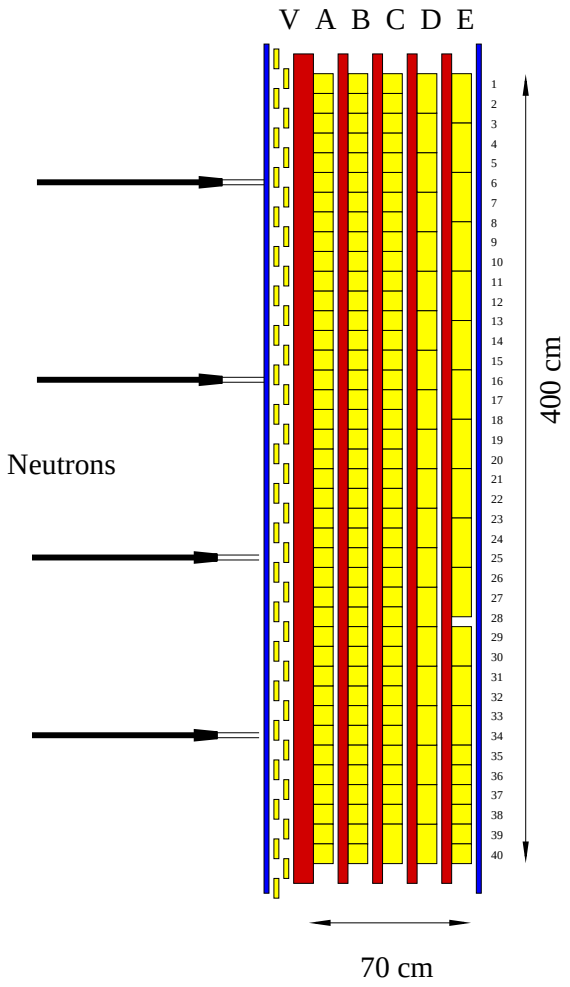

Figure 19: Side view of the neutron detector. The scintillator bars are shown in yellow, the iron converter plates in red.

4.4.2 Parameters of the Neutron Detector

The solid angle of the neutron detector is approximately 100 msr at a distance of 8 m from the target. The aspect ratio is 1:2.5. With such a geometry, the acceptance of the neutron detector matches the acceptance of the BigBite spectrometer for events up to $p_{mperp} \approx 150$ MeV/c.

The time resolution is expected to be 0.3 ns (σ). This value has been achieved routinely with the counters under consideration [61]. At a distance of 8 m, the 0.3 ns time resolution leads to a neutron momentum resolution of 250 MeV/c for a neutron momentum of 2.58 GeV/c.

The horizontal intersection point of the neutron with the neutron detector will be determined utilizing the time difference between the two phototubes of each neutron detector, while the vertical intersection point will be defined using the segmentation of the neutron detector. Based on MC simulations and experience from other experiments [26, 61] using

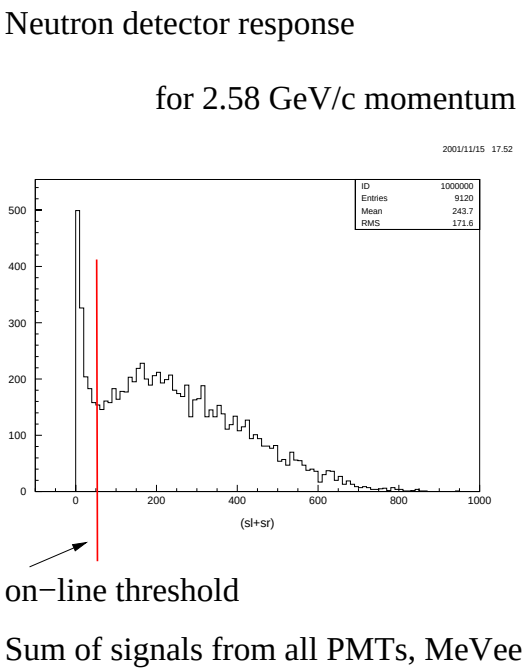

Figure 20: The results of the MC simulation for the total amplitude from all PMTs of the neutron detector.

the same counters, we expect a resolution of 5 cm in both directions. Figure 20 shows the amplitude distribution of the summed signal from all PMTs of the neutron detector. The neutron detection efficiency versus threshold for four values of the neutron momenta is presented in Table 1. The position resolution presented in this table was found from the ratio of the left and the right amplitudes, which is another method to determine the position of the shower.

4.4.3 Expected Background Rates and Shielding

In the proposed experiment the 12 μA electron beam will pass through a 40 cm long ^{3}He target. The total thickness of the glass entrance and exit windows is 240 μm. Therefore, a luminosity of $5 \cdot 10^{36}$ electron-nucleon/s/cm^2 is used for background estimates. Because the diameter of the target cell is only 2 cm and because the detectors are both located at relatively large angles (25° and 50°) it will be possible to collimate the entrance and the exit windows without significant loss of useful target length. Such a collimation will reduce the background rate in each arm (the neutron detector and BigBite) by a factor of two. However, in the following analysis the effect of these collimators was not taken into account, so the actual background could be up to two times smaller than estimated here.

The beam also passes through two Be vacuum windows (total thickness 0.5 mm) and two Al windows at the target chamber (total thickness 0.25 mm). The total amount of material in the windows is about 160 mg/cm^2. These windows can not contribute to the rate in BigBite because of its limited acceptance. We also plan to install thick lead collimators around each

of these windows in the direction to the neutron detector. In the following analysis, possible leaks through the last collimators were not included.

A MC simulation [58], which was confirmed in several measurements [62], allows the prediction of the yields of various particles. The MC was done for an incident beam energy of 3.5 GeV on the Hall A polarized ^{3}He target, which includes the ^{3}He gas, two 0.12 mm glass windows and the 1.3 mm side walls. Figure 21 shows the neutron yield. The online rejection of the background will be done by setting a threshold of 50 MeVee for the sum of the PMT signals. Pions and protons contribute most to the trigger rate of 500 kHz (for a threshold of 50 MeVee). In the analysis, the use of information from the veto counters and of high thresholds on the value of the total signal in the neutron counters (150 MeV for the highest Q^2 point) allows the reduction of the rate to the level of 10 kHz, where neutrons and pions will contribute evenly.

As was discussed in the BigBite section, the expected trigger rate on the electron arm is about 200 kHz. The coincidence time window will be 25 ns. A rate of 500 kHz for the hardware neutron trigger will lead to an acceptable DAQ rate of 2.5 kHz.

While the detector is shielded from the direct flux of particles produced at the target by a 2 cm iron plate (see above), the installation of similar shielding on the other sides could reduce the rates in the PMT's even further.

4.4.4 Veto Detector

Plastic scintillator counters will be used to distinguish neutrons from protons. The flux of low energy electrons, which will dominate the rate in the veto paddles, can also be found from MC simulations. The rate of electrons with energies above 10 MeV in one paddle of the veto detector (2.5 msr) will be 23 MHz; for electrons with energies above 30 MeV it will be 1.5 MHz. With an energy threshold of 0.5 MeV in the discriminator of the veto detector, which is protected by 2 cm of iron, the probability of detecting an electron with an incident energy of 10 MeV is 1.2%. The same parameter for electrons with 30 MeV incident energy is of the order of 10%. As a result, the expected rate in one veto counter can be estimated to be below 0.5 MHz. Such a rate coupled with a 25 ns dead time per pulse leads to a total electronics dead time of the veto detector on the level of 1.25%. A further reduction of this dead time would require a second set of veto detectors oriented vertically.

4.4.5 Veto Efficiency for High Energy Protons

The reaction $^3He(e,e'p)$ has a few times higher rate than the reaction $^3He(e,e'n)$. The standard way to distinguish between these two processes is based on the use of plastic veto counters. The p,n charge exchange reaction, which can take place in the material between the target and veto detector, can compromise the effectiveness of this approach. In the proposed experiment the materials between the ^3He target and the veto detector are: the glass of the target cell (0.7 g/cm^2), the windows of the scattering chamber (0.1 g/cm^2), the air on the 8 meter long flight path to the detector (1 g/cm^2), and the 2 cm iron protection plate (15.6 g/cm^2).

From MC simulations we found that the 2 cm iron protection wall in front of the veto detectors will introduce a 0.5% loss of detection efficiency for 2.6 GeV/c protons. The

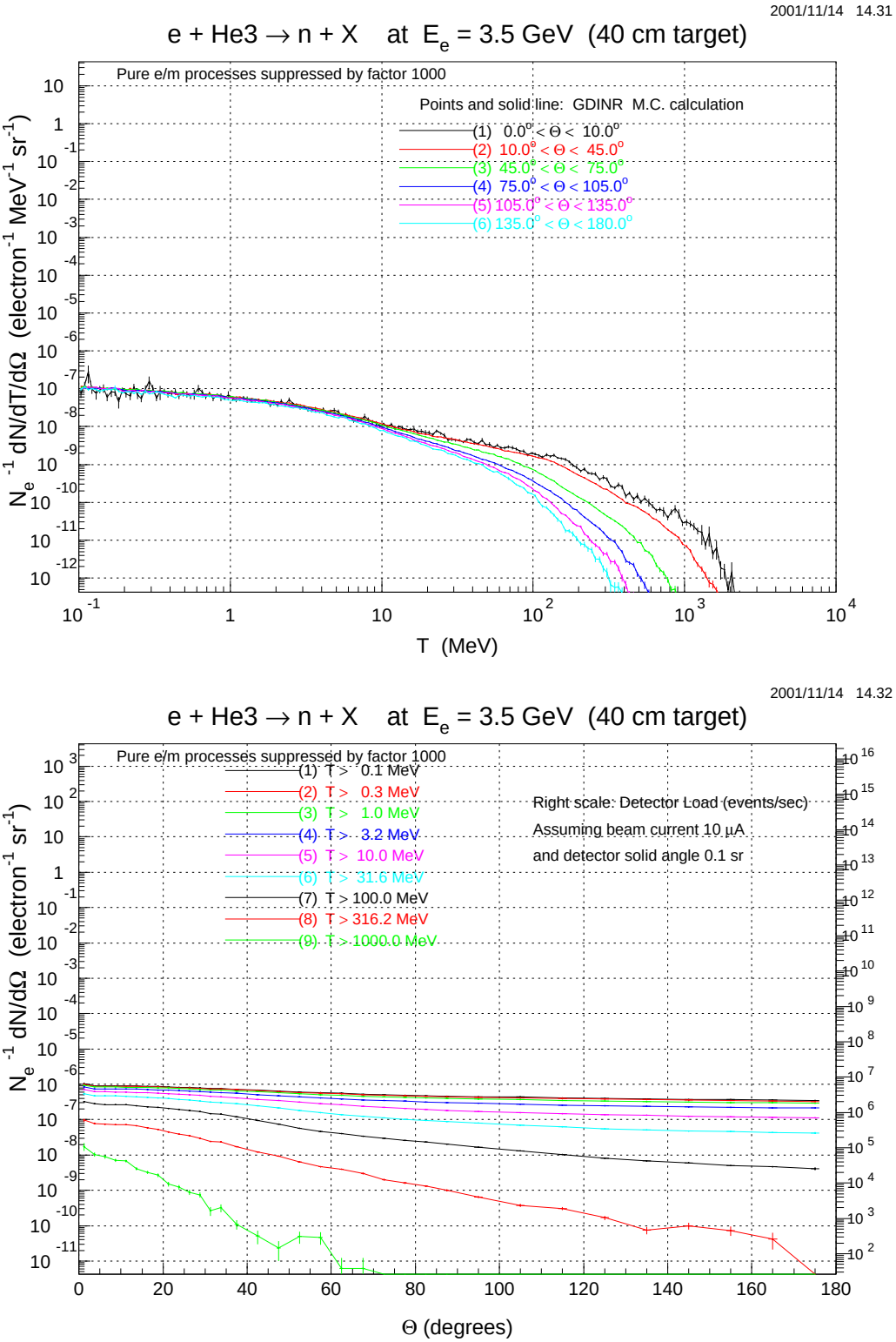

Figure 21: The neutron yield with kinetic energy above given thresholds.

probability of a hadronic interaction of the proton with the iron wall is about 15%. Such a small loss of detection efficiency is due to signals from secondary particles. The upper limit for effects from other materials is 1% based on the total probability of hadron interactions and the acceptance of the neutron detector.

4.4.6 Trigger and Front–End Electronics

The logic of the summing electronics is presented in Fig. 22. The individual PMT signal will be sent to a customized Fan-in-Fan-out/discriminator-sum unit. This unit will accept up to 16 signals from PMTs, produce logical pulses for the timing measurement of each PMT, provide analog signals for ADC analysis and output a summing signal S. Because most of the hadronic shower is contained in an area 40 cm wide, we will use the sum of two signals like S1 and S2 and send it to a discriminator D1. The groups overlap to avoid any loss of detection efficiency. The output signal of the coincidence between D1 and the meantimer MT1 will be used as a clean and accurate timing signal. Nineteen such signals will be summed again in a logical OR to make the neutron trigger. The use of a separate sum for the left and right groups and meantimers allows us to reduce the walk of the neutron trigger signal and enables the use of 25 ns gates for the coincidence with the electron arm. The veto counters are not used in the trigger logic, however they have the same type of TDC and ADC connections. The signals from all PMTs will be digitized by ADCs and TDCs.

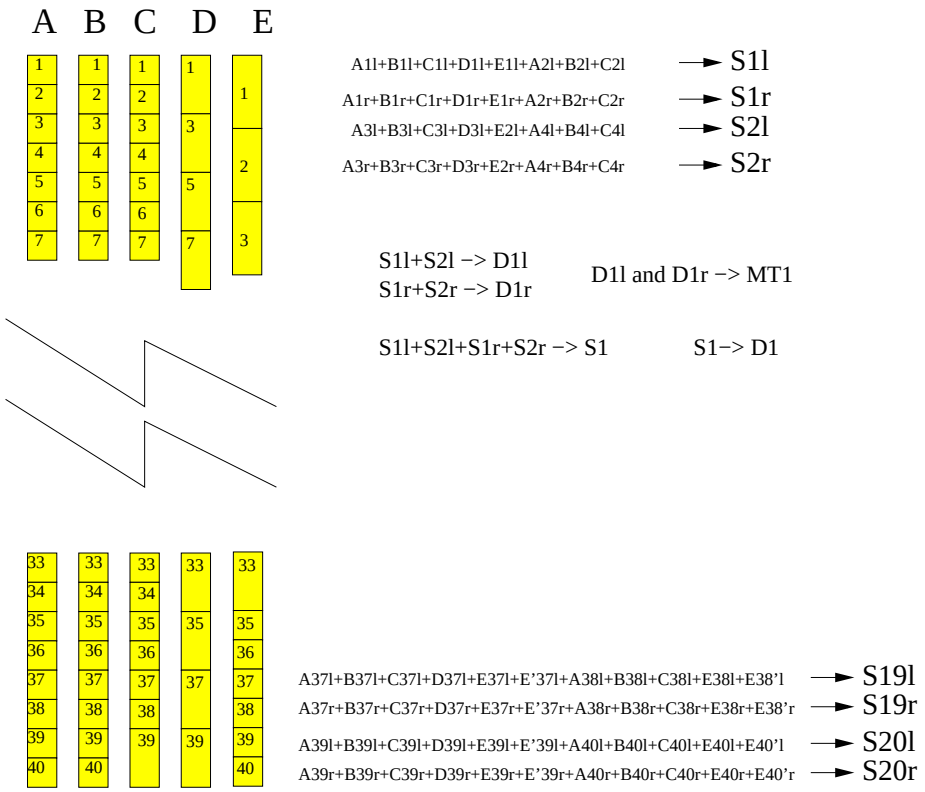

Figure 22: Layout of the neutron detector trigger logic.

$P_n, GeV/c$	A_{thr}, MeVee	50	100	150
0.80	η,%	30	15	5
1.35	η,% σ_{pos},cm	**56** **9.2**	40 8.2	27 7.2
2.00	η,% σ_{pos},cm	73 8.2	**62** **8.2**	51 7.9
2.58	η,% σ_{pos},cm	79 8.5	71 7.9	**60** **7.5**

Table 1: Neutron detection efficiency η and position resolution σ_{pos} versus threshold for P_n = 0.80, 1.35, 2.00, and 2.58 GeV/c.

5 Helicity Asymmetry in $^3\vec{H}e(\vec{e},e'n)$ and the Ratio of G_{En}/G_{Mn}

A full analysis of this subject requires calculations which are presently under development in Refs. [63, 64, 65]. Below we summarize the topics which are important ingredients in these calculations or will be used to provide consistency checks and show preliminary results of the calculations from M. Sargsian.

5.1 Nucleons in the Nuclear Medium

There are several processes related to the influence of the nuclear medium on the structure of a bound nucleon. One of the best known is the nuclear EMC effect, which shows that the structure function of the nucleus is suppressed at large x_{Bj} relative to that of the deuteron. While a definitive explanation of this effect is still elusive, it is clear that a quantitative description of the effect requires, in addition to the conventional nucleon and meson degrees of freedom, some dynamical effects involving sub-nucleonic degrees of freedom (see e.g. [66, 67, 68, 69]). However, *two factors make the EMC effect controllable in the proposed measurement.* First of all, in models where the EMC effect is proportional to the virtuality of the bound nucleon, which would potentially lead to a distortion of the intrinsic structure of the bound nucleon, the restriction to small values of missing momenta will substantially suppress any such distortion and the corresponding onset of the EMC effect. Secondly, the measured asymmetry will be less sensitive to nucleon structure modifications since the bulk of the EMC effect will be less revealed in the form factor ratios.

Color Transparency (CT) is the next effect (see e.g. [70]) which can potentially hinder the extraction of the neutron form factor at high Q^2. This effect has been investigated in quasi-elastic proton knock-out by electrons from nuclei for Q^2 from 1 to 8 (GeV/c)^2 [71]. Such studies probe the propagation of the nucleon through nuclei and test the effect of the nuclear medium on the proton knockout cross section. The aforementioned experiment [71] observed no signature for CT up to Q^2=8 (GeV/c)^2 in the kinematics of restricted missing momentum and energy. Moreover, the comparison with theoretical calculations demonstrated that the Glauber approximation adequately describes the data for a wide range of nuclei (ranging from the Deuteron to Iron). Thus for the Q^2 of the present proposal, one expects that the Glauber approximation will reliably describe the final state interactions in the $^3He(e,e'N)$ reaction.

A study of polarization observables in the reaction ^{4}He($\vec{e}$,e'$\vec{p}$) was made recently at Mainz [72] and up to $Q^2 = 2.6$ (GeV/c)^2 at JLab [73]. These experiments found that the ratio of the components of the polarization of the recoiling proton P'_x/P'_z is smaller than the same ratio for the hydrogen target by about 10% (see Fig. 23). The same effects which contribute to this modification need to be taken into account for the analysis of $^3\vec{H}e(\vec{e},e'n)$. The lower density of a ^{3}He nuclei compared to a ^{4}He nuclei will lead to a proportional reduction of these medium effects. Calculations from J. Udias predict a reduction of the ratio P'_x/P'_z of 8% in ^{4}He compared to hydrogen, whereas in ^{3}He the reduction is only a 4% effect [64].

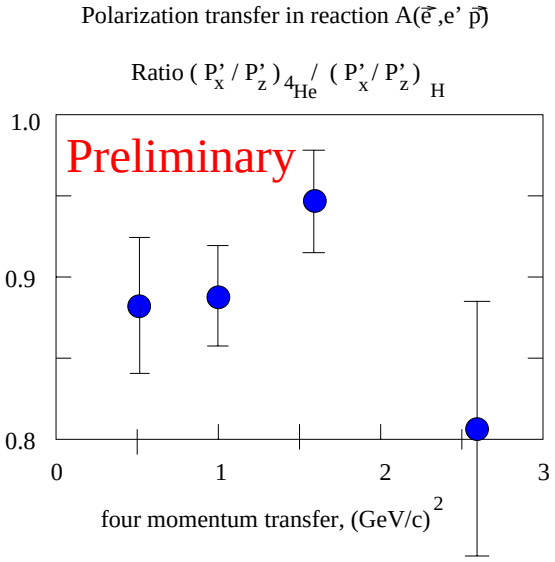

Figure 23: The ratio of the polarization transfer components for a bound proton relative to the free proton.

5.2 $^3\vec{H}e$ as a Neutron Target

Experiments utilizing $^3\vec{H}e$ targets as effective neutron targets have been carried out for a wide range of beam energies at Bates, Indiana, NIKHEF, Mainz, HERMES, SLAC and, for the last three years, in JLab Hall A. During the past decades there have been several theoretical discussions about the possibility of using a $^3\vec{H}e$ target to study the properties of the elastic electromagnetic form factors of the neutron (see Refs. [11, 53, 74]). In addition, calculations for inclusive and exclusive electron scattering reactions from $^3\vec{H}e$ have been performed in Refs. [74, 75, 76, 77].

The neutron polarization in $^3\vec{H}e$ and the three-nucleon wave function have been computed by a number of authors using several different methods, including the approach via Faddeev equations [78], and the variational approach [47, 49, 50, 51, 52, 79]. These are now well established, and the error introduced through uncertainty in the wave functions will be very small. Calculations for inclusive and exclusive electron scattering reactions were performed in Refs. [74, 75, 76, 77].

The semi–exclusive reaction $^3\vec{H}e(\vec{e},e'n)$ allows one to fix the values of the missing momenta and energy of the struck neutron which are the key parameters for controlling the size of nuclear effects. A cut on the transverse components of the neutron momentum p_{mperp} is more effective in this task than a cut on the longitudinal component p_{mpar} [63]. In the proposed experiment the value of the asymmetry will be measured as a function of p_{mperp} in the range 0–150 MeV/c. This will allow us to check the universality of the result and to extrapolate to low p_m^2.

5.3 Qualitative Assessments of Nuclear Effects in the Extraction of G_{En}/G_{Mn} from Semi-exclusive $A(e,e'N)X$ Reactions

The key observation driving the proposed measurement is that it is possible to select small momenta in the ^{3}He wave function by requiring p_{mperp}<30 MeV/c. This is the case because the good convergence of the integral $\psi(k)dk$ (normalized as $\int \psi^2(k)d^3k = 1$) leads to the selection of very small momenta in the wave function of ^{3}He, even though the cut on p_{mpar} is rather modest (250 to 500 MeV/c). In our kinematics the effective cut on missing energy E_m is almost the same as the cut on p_{mpar}.

Additionally, these cuts ensure the suppression of the proton polarization, which is already a small factor ($< 3\%$), and suppress small non-nucleonic admixtures in the wave function. Furthermore, they significantly suppress the final state interactions, since the struck nucleon is rather far from other nucleons. Besides, most of the rescattering in these kinematics actually removes nucleons to larger transverse missing momenta p_t, and hence they do not affect asymmetries calculated in the PWIA in order to extract $R = G_{En}/G_{Mn}$.

The following is the assessment of nuclear effects that may affect this extraction, and some qualitative estimations indicating which corrections will be possible to estimate more quantitatively.

1. Finite acceptance effects. Because the experiment will measure G_{En} within a finite interval of missing momenta p_m and missing energy E_m, the integration will smear out the extracted R. This effect is expected to be small if a tight cut on the p_{mperp} and a modest cut on E_m are applied.

2. Off-shell effects. The uncertainty associated with off-shell effects can be estimated by applying the different off-shell prescriptions for calculation of nucleon currents. However, since the momenta of the struck nucleons are small, these effects, which are proportional to p_m^2/m_N^2, should be strongly suppressed.

3. Meson Exchange Effects. The choice of high Q^2 causes a significant suppression of meson exchange effects in the extraction of R. At $Q^2 > 1$ (GeV/c)^2 the overall additional Q^2 dependence of the MEC amplitude as compared to the PWIA amplitude will be $(1 + Q^2/\Lambda^2)^{-2}$, where $\Lambda^2 = 0.8 - 1$ (GeV/c)^2(see e.g. [63]). Additionally, the MEC contribution will be suppressed due to the restriction of small p_{mperp} and E_m (usually MEC effects start to contribute at rather large nucleon momenta, of the order of 300 MeV/c). One way to estimate these effects is to take the theoretical calculations at small Q^2 and scale them according to the relation given above.

   The proposed experiment will take data at $Q^2 = 1.31$ (GeV/c)^2, where the measurements from Refs. [26, 27] were performed utilizing a deuteron target, so the experimental evaluation of nuclear effects can be performed.

4. Delta Isobar Contribution. This effect should be small because of the restrictions on p_m and E_m. If one assumes the same Q^2 and energy dependence of the elastic electromagnetic form factor as of the $N\Delta \to NN$ rescattering amplitude, one is able to estimate the Δ contribution using the FSI amplitude but taking into account the fact

that it corresponds to the larger p_{mpar} in the argument of the nuclear wave function. This gives the upper limit of the Δ contribution.

Pre-existing Δ-isobars in ^{3}He have a rather small probability – about 2% – and they also have substantially larger average transverse momenta than nucleons. Hence the cut on small average nucleon momenta will lead to further suppression. Still this is a potential background since there can be a transition $\gamma^*\Delta^0 \to n$. One should remember that the Δ^0 is polarized. From the violation of the Bjorken sum rule one can expect the Δ contribution integrated over all momenta to be on the level of 4% times the ratio of the ΔN form factor and the NN form factor. An additional small factor mentioned above is the cut on momenta – so qualitatively one may get an effect on the scale of 1-2%.

5. Final State Interactions. The major advantage is that at high Q^2 the eikonal approximation is applicable when the rescattering amplitude is practically energy-independent. First we discuss FSI due to diagonal $np \to np$ rescattering. In the case of the factorized approximation the uncertainty comes from the accuracy of the calculation of FSI contributions, which is less than 10%. The recent comparison of eikonal calculations with JLab data demonstrated very good agreement for Nuclear Transparency starting with the Deuteron and going up to Iron [71].

   In the case of small p_{mperp} and E_m, the overall effect of FSI for the ^3He target is 10-15%, thus the uncertainty due to the accuracy of FSI is 1-1.5%. The theoretical calculations will all allow an estimation of the uncertainty due to factorization.

   Nondiagonal FSI is due to charge exchange rescattering.

   In the high energy limit the charge exchange amplitude pn to np is mainly real. The imaginary part at Q^2 = 1-1.5 (GeV/c)^2 is 10-20% of the diagonal amplitude, thus one expects that charge-exchange will contribute 1-2% in the overall FSI. The real part will contribute in the non-eikonal part of the rescattering as well as in the double rescattering. There is an additional small factor in the asymmetry amplitude since the proton is polarized very weakly in the kinematics chosen for the measurements. Since charge exchange goes through the pion exchange its amplitude decreases with s (compare the s-independence of diagonal $NN \to NN$ amplitude). The theoretical calculations will allow an estimate of this contribution.

To summarize, it appears that corrections to the impulse approximation will be significantly less than 10% (expected on the level of 2-5%), and most of these effects will be possible to correct for. The code will also provide the extraction algorithm which will allow an extraction of R taking into account FSI terms.

5.4 Preliminary Results of the GEA Calculation

GEA [63], a code based on the generalized eikonal approximation, was used for the calculations of A_{perp} shown in Fig. 24. The asymmetries were calculated for a beam energy of 3.244 GeV and assuming that G_{En} follows the Galster parameterization. The following cuts on the components of missing momenta were applied: p_{mperp} less than 50 MeV/c and

p_{mpar} less than 250 MeV/c. The invariant mass cut was $W = 0.94 \pm 0.05$ GeV. The upper solid line presents the results of the code for a free neutron at rest. The lower solid line with smaller values of A_{perp} is a naive estimate of the asymmetry based on the neutron carrying 82% of the polarization of $^3\vec{H}e$. The dash line presents the results of the PWIA calculation. The dotted line is the results of the DWIA calculation. The dash-dotted line presents the DWIA calculation with Charge Exchange (CE) effects included. The effect of CE is about 5.5% at Q^2= 1 (GeV/c)^2 and drops to 3.6% at Q^2= 4 (GeV/c)^2 , in agreement with our expectations.

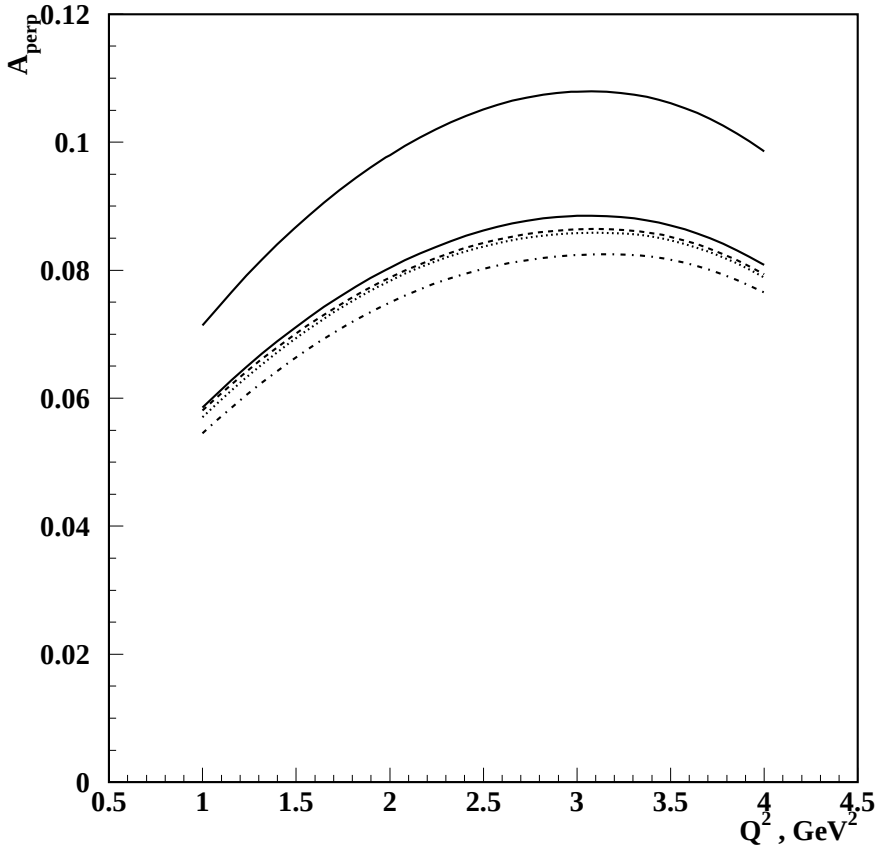

Figure 24: The A_{perp} asymmetry calculated by Sargsian in the generalized eikonal approximation. The upper solid line presents the result for a free neutron at rest. The lower solid line with smaller value of A_{perp} is a naive estimate of the asymmetry based on the neutron carrying 82% of the polarization of $^3\vec{H}e$. The dash line presents the results of the PWIA calculation. The dotted line is the results of the DWIA calculation. The dash-dotted line presents the DWIA calculation with CE effects included.

6 Quasi-Elastic Scattering at Q^2 of Several (GeV/c)^2

In this section we will discuss the physics and room background contributions to the data and the method of separating the quasi-elastic scattering (QES) events from the background. Several physics processes contribute to the background which the detectors will see, including inelastic scattering associated with pion production, single pion photo-production and quasi-elastic scattering from the protons in $^3\vec{H}e$. Inelastic scattering associated with pion production will be discussed in the first subsection. Single pion photo-production by virtual photons can be suppressed by using particle identification, as discussed in the second subsection. The suppression of quasi-elastic scattering from the protons in $^3\vec{H}e$ requires a high efficiency of the veto detector in the neutron arm and will be discussed in the third subsection. The room background in the data comes from accidental coincidences due to the high rates of low energy neutrons and pions, which will be discussed in Sec. 6.4.

6.1 Selection of the QES Events

The first step of an extraction of G_{En} is the selection of the quasi-elastic scattering events. Previous proposals used MC simulations of QES and pion production to evaluate background contributions. We used experimental data from the ^{3}He(e,e′p) reaction measured with the Hall B CLAS detector at an incident beam energy of 4.4 GeV to study the effects of restrictions on missing momenta on the selection of QES events [80]. *The resolutions achieved in this Hall B experiment are better than what we will achieve in the proposed setup. However, in the following analysis all cuts are chosen in a way which can easily be realized for the analysis of the data from the proposed measurement with the projected momentum and angular resolutions.*

The upper part of Fig. 25 shows the inclusive electron spectra at two values of Q^2, which are close to the proposed measurements. The plots show the event distributions as a function of the final electron energy. In the lower part the same data are shown, but as a function of invariant mass $W = \sqrt{m_N^2 + 2m_N(E - E') - Q^2}$. In the inclusive spectra for Q^2=3.5 (GeV/c)^2, the QES peak appears as a very small contribution to the spectra intensity near W=1 GeV. However, if one looks at the coincidence data in Fig. 27, the spectra are much cleaner. The figure displays the p_m distribution for five ranges of W. For $W = 0.95 \pm 0.1$ GeV the peak at low p_m dominates. In the range $p_m < 250$ MeV/c the level of non-QES contributions is below a few percent. These pictures show how the inelastic contribution grows with increasing W.

The details of the spectra for $W = 0.95 \pm 0.1$ GeV at low values of p_m are shown in Fig. 26, where the QES peak was fitted by the function $p_m^2 exp(-p_m^2/(2p_a^2))$ and the non-QES part by the function $p_m^2/(1 + p_m^2/p_b^2)$.

Figure 28 shows the event distribution versus the value of p_{mperp}, which is the part of the nucleon momenta perpendicular to the momentum transfer vector $\vec{q}$. In this figure, a loose cut on p_{mpar} was applied ($\leq$0.5 GeV/c), which is the part of the nucleon momenta parallel to the momentum transfer vector $\vec{q}$. Here the peak was fitted by the function p_{mperp} exp(-$p_{mperp}{}^2/(2\mathrm{p}_a^2)$) and the non-QES part by the function $p_{mperp}{}^2/(1+p_{mperp}{}^2/\mathrm{p}_b^2)$.

Our MC simulations show that detector setup will provide a W resolution of 50 MeV, a

p_{mpar} resolution of 250 MeV/c, and a p_{mperp} resolution of 30 MeV/c. These parameters will allow us to do a data analysis similar to the one described above for the CLAS data. The quality of the separation between QES and non-QES events will be the same as shown in Fig. 28. In this case a clean extraction of QES events will be possible, and the background remaining from non-QES events will be less than 5%.

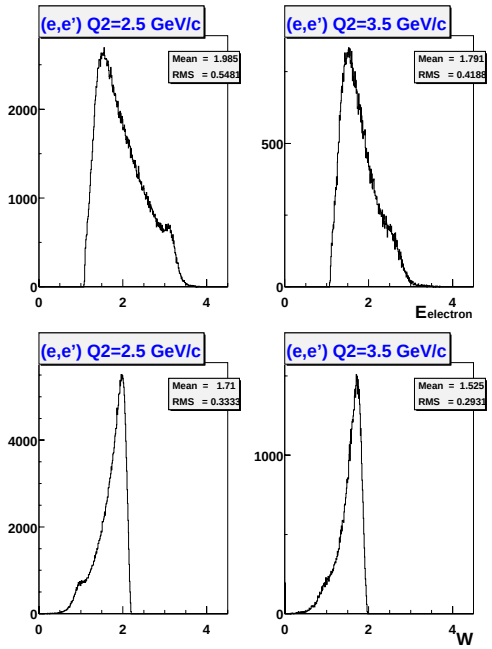

Figure 25: The inclusive electron spectra for the reaction $^3\vec{H}e(e,e')$ at an incident energy of 4.4 GeV for two values of Q^2. The lower graphs are the invariant mass distributions. The scales are in GeV.

The analysis shown above is focused on the range of $W = 0.95 \pm 0.1$ GeV, which contains about 60% of all QES events. To get nearly all of the QES events it is necessary to analyze data for W up to 1.15 GeV. The scan of W from 0.45 to 1.25 GeV confirms that it is possible to use events with W from 0.45 up to 1.15 GeV after applying cuts on the missing momenta p_{mpar} (see Fig. 28). The asymmetry in the background events will be analyzed in the large p_{mperp} region.

6.2 Photo-Production of Charged Pions

For estimating the photo production rate of positive pions from the $^3\vec{H}e$ target we used the value of the cross section from free protons and took the number of protons in ^3He into account. In the photon energy range above 2 GeV and at large θ_{CM}, the cross section for single pion production is $d\sigma/dt \approx 20mb/s^7$, where t is a momentum transfer and s is $m_N^2 + 2m_N E_\gamma$ in $(\mathrm{GeV/c})^2$. In this reaction particles have almost the same kinematical correlations as in QES. The range of photon energies which need to be considered is defined by the acceptances of the two detectors. The angular correlation between the pion and neutron leads to a cutoff of coincidences at photon energies below 2.1 GeV (here we are considering the case at the highest Q^2 point with an electron beam energy of 3.244 GeV).

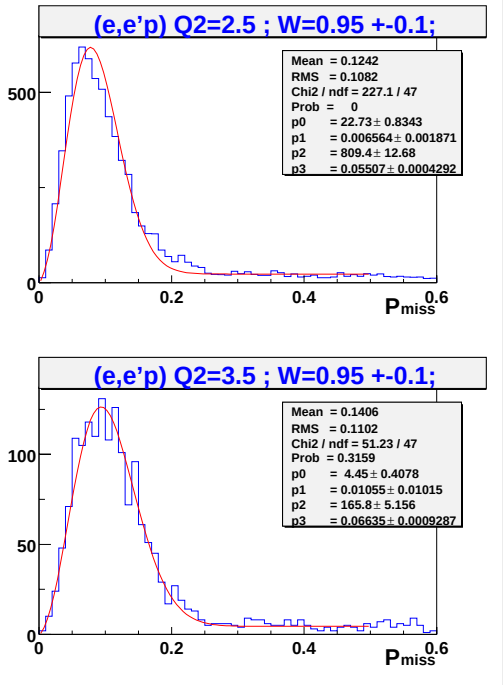

Figure 26: A fit of the p_m distributions for $W = 0.95 \pm 0.1$ Gev/c. The scales are in GeV/c.

The intensity of real and virtual photons at $E_\gamma = 2$ GeV and higher was estimated to be 0.5% of the electron beam intensity times dE_γ/E_γ. The total rate of pion-neutron events was found to be on the order of 30 Hz. Pion rejection will be performed off–line by means of the lead glass shower counter (a factor of 100) and rejection based on the track analysis, because of the positive curvature for π^+ tracks (a factor of 50, limited by background hits in the MWDC). An additional reduction by a factor of 2 comes from the analysis of the correlation between the pion momenta and the lead glass signal. The resulting rate of 0.003 Hz corresponds to a 0.7% contamination of the sample of QES events.

Negative pion production from the neutron in $^3\vec{H}e$ leads to a two-times smaller rate of events with a high energy proton in the neutron detector. Such events will be rejected by means of the veto detector on the proton side (factor of 30-50) and the lead glass counter on the pion side (factor of 100).

The background from the glass windows of the target cell and other windows will be cut–out in the analysis by using cuts on the reconstructed coordinate along the target.

6.3 QES from the Protons in $^3\vec{H}e$

The rate of QES from the bound protons in $^3\vec{H}e$ is about factor of four–five higher than in the process under study. The use of plastic scintillator counters as a veto detector is a well developed technique. The veto detector can be segmented because of the good spatial resolution of the neutron bars, which enables the localization of the area where the check in the veto needs to be performed. The segmentation of the veto reduces the rate per detector and solves the problem of electronics (and PMT) dead time. Still, at the luminosity of this

proposal the veto detector inefficiency is expected to be 1-1.5%. This parameter will be measured during the experiment by using the second layer of the veto which covers only a small portion of the neutron detector and is used mainly for the measurement of the veto efficiency. The remaining background will be on the level of 5%. The protons in $^3\vec{H}e$ have a low polarization so such background is much less important than in case of G_{En} experiments using deuteron targets. Because the efficiency will be measured, the contribution of this background to the systematics in the asymmetry measurement is about 1-1.5%.

The nuclear interaction of the protons with the material between the target and the veto detector was discussed in the neutron detector section. It will lead to an inefficiency of 0.5%.

6.4 Accidental Background

The DAQ rate is expected to be on the level of 2.5 kHz with a coincidence time window of 25 ns. This rate corresponds to a 50 MeV threshold in the neutron arm and triggering of the electron arm from a two layer plastic scintillator trigger plane. The off–line analysis will use a 150 MeV threshold in the neutron arm and the lead glass shower detector for suppression of the pion events in BigBite. This analysis will bring the rate to 10 kHz in each arm. The 2.5 ns time window will reduce the rate of accidentals to 0.25 Hz. The fraction of background events within the range of p_{mperp} from 0 up to 150 MeV/c is 11%. The irreducible rate of 0.027 Hz corresponds to a 6% background for detected $^3\vec{H}e(\vec{e}, e'n)$ events. Because of several means to measure the amount of background of this type, its contribution to the systematics of the asymmetry measurement will be on the level of 1%.

6.5 Analysis of the Raw Asymmetry and Extraction of A_{perp}

The raw helicity asymmetry in the rate of QES electron-neutron events in a given range of Q^2 and p_{mperp} will be corrected for the degree of polarization of the $^3\vec{H}e$ nuclei in the target, for the beam polarization, for the dilution factor, and also for the background asymmetry. The result of this first analysis step is A_{phys}, which has contributions from both A_{long} and A_{perp} because of the large angular acceptance of the electron arm. The systematics of the A_{long} calculation are expected to be on the level of 0.001 for an angular alignment accuracy of 1 mr. The averaged value of A_{long} is expected to be -0.007, which is about 15 times smaller than A_{perp}, which is expected to be about 0.108 (see Sec. 4.3). A_{long} will be calculated based on the direction of the target polarization and the acceptance of BigBite. The averaged A_{phys} corrected for the acceptance factor allows the extraction of A_{perp} with a systematic uncertainty smaller than 1%. The next step is to relate the value of A_{perp} to A_T for the free nucleon (see Sec. 5).

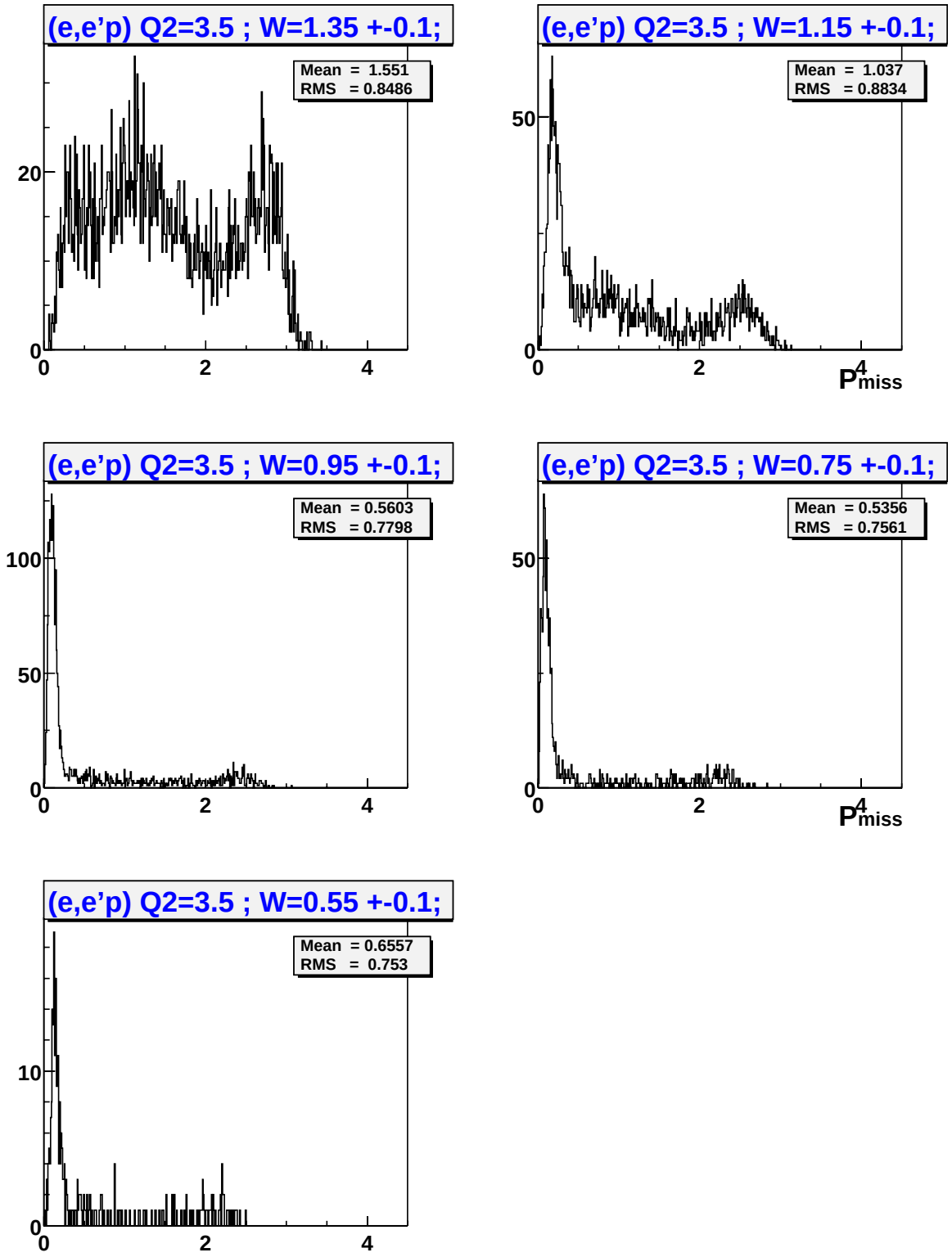

Figure 27: The p_m distributions for $^3\vec{H}e$(e,e'p) at Q^2 of 2.5 (GeV/c)^2 and 3.5 (GeV/c)^2 for five W values. The scales are in GeV/c.

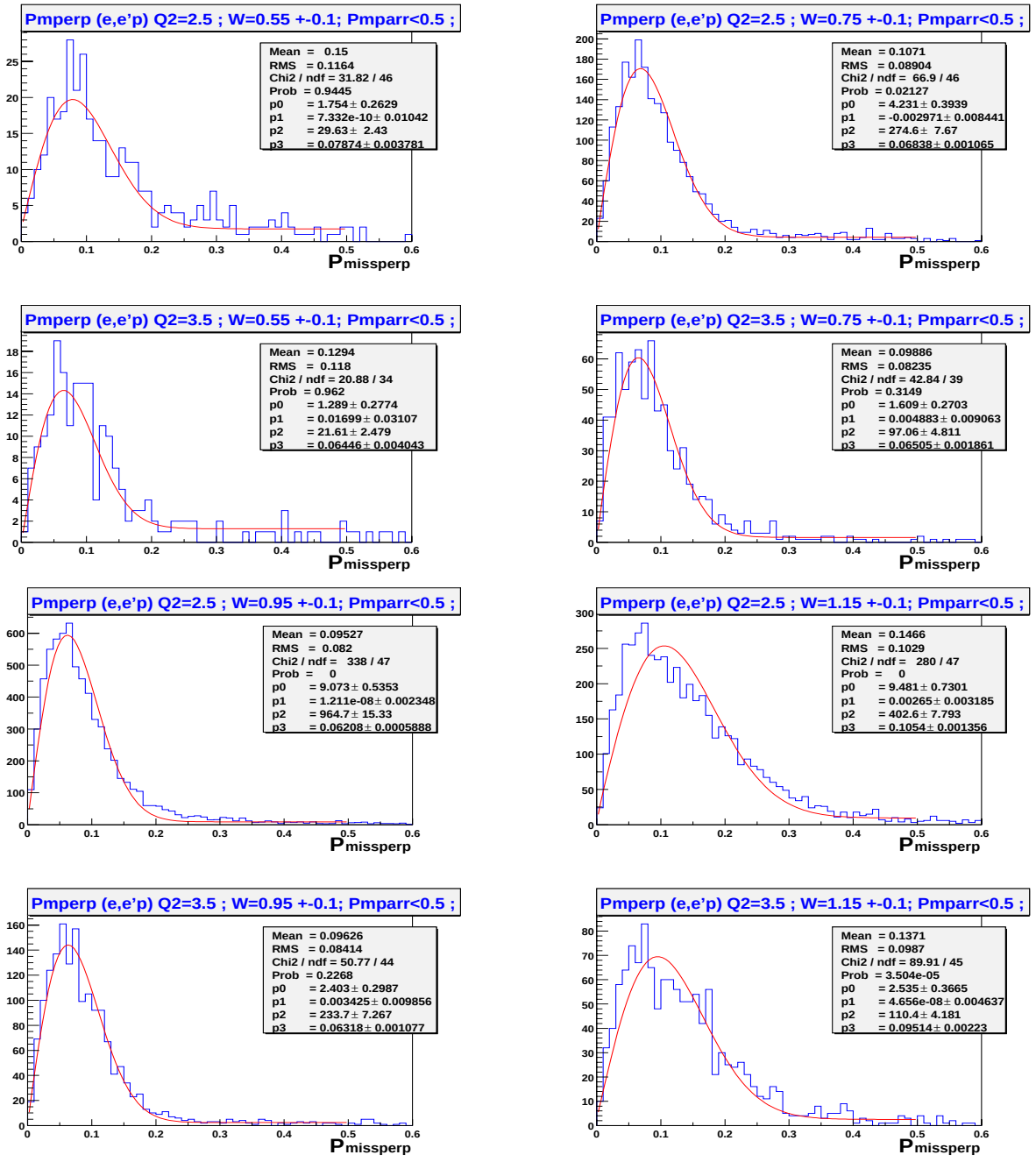

Figure 28: The fit of p_{mperp} distributions for four W ranges with the cut on p_{mpar} . The scales are in GeV/c.

7 Proposed Measurements

7.1 Kinematics

To choose which is the best combination of beam energy and scattering angle to measure G_{En} for a given Q^2, one has to evaluate the Figure-of-Merit (FOM). In our case, the FOM is given by

$$FOM = R(\theta) / \left(\partial \left(G_{En}/G_{Mn}\right) / \partial A_{perp}\right)^2 , \tag{13}$$

where $R(\theta)$ is the counting rate, which itself is proportional to the cross section times the effective target length and the acceptance of the particular spectrometers used. In Fig. 29 the FOM is plotted as function of the beam energy at a fixed Q^2 of 3.4 (GeV/c)^2. The upper two curves show the FOM using the BigBite spectrometer, the lower set of curves using the HRS spectrometer as electron detector. To study the influence of the value of G_{En} itself, the FOM has been calculated assuming that G_{En} follows the Galster approximation and assuming that it is four times larger. For a given Q^2, the FOM increases for higher beam energies, which corresponds to detecting the electron at smaller scattering angles. The variation of G_{En} does not change the general behaviour of the FOM. The difference between the FOM for the HRS and for BigBite reflects the different solid angle and the different transverse acceptance of the two devices. The maximum momentum for electrons in the BigBite spectrometer is

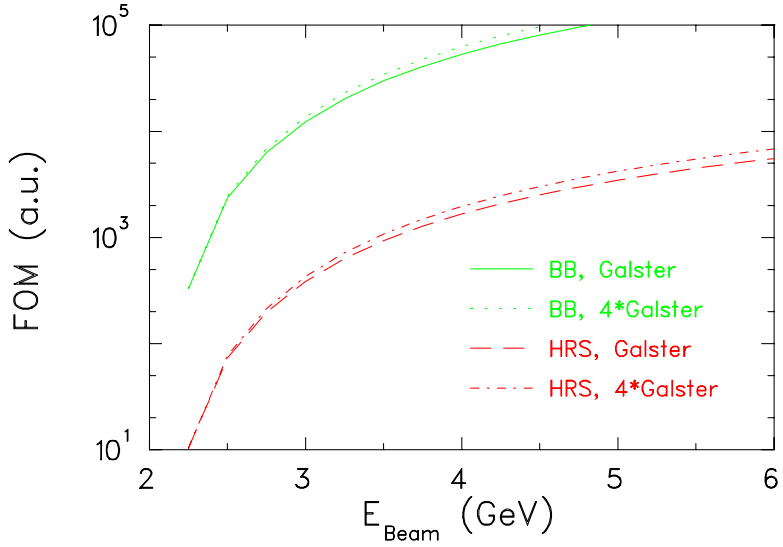

Figure 29: The FOM as function of the beam energy at fixed $Q^2 = 3.4$ (GeV/c)^2. An increase in the beam energy translates into smaller electron scattering angles and higher momenta of the recoiled electron.

1.5 GeV/c, which limits the scattering angle to values above 50° and the beam energy to roughly 3.3 GeV for a Q^2 of 3.4 (GeV/c)^2. Although the HRS spectrometer would allow us to go to more forward angles, the FOM would nevertheless be smaller than with the BigBite spectrometer due to its smaller solid angle. The other two kinematics were chosen so that the beam energy can be changed by changing the number of passes in the accelerator. Table 2 summarizes the proposed kinematics.

Q^2 (GeV/c)^2	E_i GeV	θ_e deg	p_e GeV/c	θ_n deg	p_n GeV/c	T_n GeV
1.31	1.644	54.6	0.95	35.2	1.34	0.70
2.40	2.444	54.6	1.17	28.3	2.01	1.28
3.40	3.244	50.6	1.43	25.4	2.58	1.81

Table 2: The three proposed kinematics.

7.2 Asymmetry and Rate Estimates

The asymmetry A_{phys} in $e-n$ scattering is related to the experimentally measured asymmetry $A_{exp} = (N_+ - N_-)/N$ via the equation

$$A_{phys} = \frac{A_{exp}}{V\ D\ P_e\ P_n}, \tag{14}$$

where $D = 0.94$ and $V = 0.91$ are dilution factors, P_e is the polarization of the beam, and $P_n = 0.86 P_{He}$ is the polarization of the neutron. In the following estimates, we assume $P_e = 0.75$ and $P_{He} = 0.40$, both of which are values which have been achieved during recent experiments in Hall A using the polarized ^{3}He-target.

The following rate estimates are based on scattering from a free neutron. Experiments to study color transparency [71] have shown that, in a wide range of nuclei, the quasi–elastic scattering cross section is reduced by a factor of $c \cdot A^{\alpha(Q^2)}$, where $c = 1$, A is the mass number of the nucleus, and $\alpha = 0.25$ for the momentum transfers proposed in this experiment, leading to a reduction of the cross section by a factor of 0.75 for ^3He. Radiative corrections further reduce the number of useful events. The correction factors for these effects are estimated to be between 0.82 and 0.85.

Q^2 (GeV/c)^2	rate (Hz)	A_{exp}	G_{En} (Galster)
1.3	13.8	-0.0295	0.0284
2.4	1.49	-0.0260	0.0141
3.4	0.45	-0.0233	0.0086

Table 3: Rate estimates for this proposal. We assume a target polarization P_{He} of 40%, a beam polarization P_e of 75%, dilution factors $D = 0.94$ and $V = 0.91$, an average beam current of 12μA, an effective target length of 25 cm/$\sin\theta_e$, and a solid angle of 76 msr for the electron arm. Furthermore, this rate is calculated assuming that G_{En} follows the Galster–approximation and that we detect the neutrons with an efficiency of 60%.

To distinguish the quasi–elastic scattering process from others, tight cuts on the missing momentum have to be applied. We expect to reduce the number of counts by a factor of 0.66 due to these cuts. As already pointed out, the asymmetry will be studied as a function of p_{mperp}. Therefore the results have to be analyzed in separate bins, each of which must include enough statistics to obtain the desired statistical uncertainty. We are planning to get events in three different p_{mperp} bins. The rates and asymmetries we expect, using these assumptions, are shown in Table 3.

7.3 Error Estimates and Beam Time Request

The uncertainty δA_{phys} can be expressed as

$$\left(\frac{\delta A_{phys}}{A_{phys}}\right)^2 = \left(\frac{\delta A_{exp}}{A_{exp}}\right)^2 + \left(\frac{\delta P_e}{P_e}\right)^2 + \left(\frac{\delta P_n}{P_n}\right)^2 + \left(\frac{\delta D}{D}\right)^2 + \left(\frac{\delta V}{V}\right)^2 . \tag{15}$$

The beam polarization in Hall A can be measured with the Compton and the Møller polarimeter to better than 3%. Both polarimeters are standard equipment in Hall A. The polarization of ^{3}He can be measured with an uncertainty of 4%, the polarization of the neutrons in ^3He is known to 2%. The combined uncertainty in D and V is estimated to be 5%. For small asymmetries, the statistical uncertainty δA_{exp} can be approximated as $\delta A_{exp} = 1/\sqrt{N}$. The corrections of the asymmetry due to contributions from A_{long} lead to an additional uncertainty of 1%. To extract G_{En} from the measured A_{phys}, equation (9) has to be evaluated. Investigating the error propagation in this equation, taking into account the complete denominator, but neglecting the second, longitudinal part, leads to

$$\left(\frac{\Delta G_{En}}{G_{En}}\right)^2 = \left(\frac{\delta G_{Mn}}{G_{Mn}}\right)^2 + \left[\left(\frac{\delta A_{phys}}{A_{phys}}\right)^2 + \left(\frac{\delta f_{nucl}}{f_{nucl}}\right)^2\right] \; C^2 \; \left(1 - \frac{1}{R}\right)^2 \; (G_{En})^{-2} \tag{16}$$

with

$$C = 2\sqrt{\tau(1+\tau)}\tan(\theta/2)\,\frac{G_{Mn}}{2A_{phys}} \tag{17}$$

and

$$R = \sqrt{1 - 4\tau\left[1 + 2(1+\tau)\tan^2(\theta/2)\right]\left(\frac{A_{phys}}{2\sqrt{\tau(1+\tau)}\tan(\theta/2)}\right)^2} . \tag{18}$$

Knowledge of G_{Mn} is mandatory. Hall B experiment E94-107 will provide data for G_{Mn} with an accuracy better than 5%. As discussed in Sec. 5, we expect the correction factor f_{nucl} for nuclear effects to be 0.85 – 1.0, and the corresponding systematic error to be below 5%. Table 4 summarizes the various contributions to the total error for the example of the highest Q^2 point.

One purpose of this experiment is to measure the ratio G_{En}/G_{Mn} with an uncertainty similar to the results on G_{Ep}/G_{Mp} achieved in E93-027. Therefore our beamtime request is chosen so that we can obtain a statistical uncertainty $\Delta G_{En}/G_D < 0.04$, which is similar to the demand $\Delta G_{En}/G_{En} < 0.14$. The resulting times are summarized in Tab. 5.

The polarization measurements, besides the Compton measurement, are disruptive, so additional beamtime is needed. To monitor the target polarization continuously, one target polarization measurement every six hours is necessary. Also, the Møller polarization measurements need additional time. There are two ways to measure the dilution factors: one way is to fill the target cell with nitrogen, the other way is to align the target spin parallel to the momentum transfer. Together we expect an overhead of 20% for these studies. During the experiment, two configuration changes are necessary. These changes include a change of the beam energy, changes of the position of the BigBite spectrometer and the neutron detector array, and adjustments of the polarized ^{3}He target. Each configuration change will take one

quantity	expected value	rel. uncertainty
statistical error in raw asymmetry A_{exp}	-0.0233	13.4%
beam polarization P_e	0.75	3%
target polarization P_{He}	0.40	4%
neutron polarization P_n	$0.86 \cdot P_{He}$	2%
dilution factor D	0.94	3%
dilution factor V	0.91	4%
correction factor for A_{long} components	0.94	1%
G_{Mn}	0.057	5%
nuclear correction factor	1.0 – 0.85	5%
statistical error in G_{En}		13.8%
systematic error in G_{En}		10.4%

Table 4: The various contributions to the total error in G_{En} for the data point at Q^2=3.4 (GeV/c)^2.

Q^2 (GeV/c)^2	time (hours)	Counts (10^3)	$\Delta A_{phys}/A_{phys}$	$\Delta\ G_{En}/\ G_{En}$ statistical	$\Delta\ G_{En}/\ G_{En}$ systematical
1.31	24	149	0.082	0.087	0.105
2.40	104	76	0.137	0.142	0.104
3.40	456	100	0.134	0.138	0.104

Table 5: Expected uncertainties for this proposal. The times given in this table are pure data taking times assuming 100% efficiency. They do not include the time needed for polarization measurements or measurements of the dilution factor. The number of counts is given for one bin in p_{mperp} after applying the cuts described in the text.

shift. We furthermore request 48 hours of beamtime for calibration runs. In total we request 768 hours of beamtime to perform the proposed measurement, as detailed in Tab. 6.

	beam energy (GeV)	data taking time (hrs)	total time (hrs)
calibration runs	1.644		48
Q^2= 1.31 (GeV/c)^2	1.644	24	30
Q^2= 2.40 (GeV/c)^2	2.444	104	128
Q^2= 3.40 (GeV/c)^2	3.244	456	546
configuration changes			16
Σ		584	768

Table 6: Beamtime request for this proposal, assuming 100% availability of the accelerator and the experimental equipment. Data taking time includes only the time for measuring G_{En}, whereas the total time also includes the time needed for polarization measurements and measurements of the dilution factor D.

8 Technical Considerations

In this part we review the technical changes or additions to the standard Hall A equipment which are required for this experiment, and estimate the cost to JLab or other sources.

Polarized ^{3}He Target

The parameters of the Hall A $^3\vec{H}e$ target are well suited to this proposal. The special feature of this proposal is the use of the large acceptance spectrometer BigBite which limits the space for the Helmholtz coils of the holding field. In Sec.4.2 a possible approach for the necessary modifications of the holding field was presented. The collaboration will continue to search for a cost effective solution of the holding field components. The collaboration will continue its efforts to increase the degree of polarization. The level of 45% may be achieved in one year, according to present bench results.

BigBite Spectrometer

The BigBite spectrometer was built at NIKHEF [55, 56] and used in several experiments with an internal target at AmPS. It has a detector package adequate for a luminosity of 10^{33} $\mathrm{cm}^{-1}\mathrm{s}^{-1}$. The counting rate capability was limited by the trigger scintillators. The existing multi-wire drift chambers can handle the singles rate expected for the proposed experiment, but need an upgrade of their DAQ for the individual readout of 338 signal wires and 328 cathode strips. The cost of this upgrade will be on the level of **$25k**. The upgrade will make it possible to have a high resolution tracking detector for a luminosity of 10^{37} cm^{-2} per sec. The BigBite collaboration is going to upgrade the trigger plane [81] as a part of the preparation of BigBite for experiments E01-014 and E01-015. The trigger plane and its electronics will be ready by summer 2002.

Neutron Detector

A total number of 176 neutron bars will be used in our setup, see Fig. 19. The front layer of the neutron detector, which consists of 40 neutron bars with dimensions of 10x10x160 cm^3, will be built with new components. The cost of these bars will be **$80k**, according to a quote from the vendors of scintillator counters and PMTs. A total number of 78 bars with dimensions of 10x10x160 cm^3 will be provided from the E93-026 experiment ("UVa bars"), under the responsibility of D. Day. A significant fraction of these bars are committed to a series of SLAC experiments. The first will run in 2004. Scheduling of the proposed experiment before 2004 will avoid extra transportation of the bars. Another 24 bars with dimensions 10x20x180 cm^3 [61] will be provided by the University of Glasgow, under the responsibility of J. Annand. The fifth layer of the neutron detector will be made of 37 counters of various dimensions. Almost all bars for the last layer will be contributed from experiment E01-015, under the responsibility of E. Piasetzky and J. Watson. In total 42 veto counters with a cross section of 1x11x160 cm^3 are needed for our experiment. Almost all of them (39) will be provided from the E93-026 experiment. At least three additional veto counters need to

be constructed. The cost of a 18 ton detector platform, which includes 14 tons of shielding, is estimated at **$20,000**.

Electronics:

Front end:

A new trigger setup needs to be built for the neutron detector. The setup will include the splitter of every PMT signal, discriminator, fanout for the ADC and summer to the trigger. We plan to develop a custom module which will combine all these functions. Similar electronics were built for the RCS calorimeter, where the trigger is based on a summed signal from the lead glass modules. The proposed modules should have, in addition to the RCS version, a leading edge discriminator for every channel. The meantimers will be used to reduce the coincidence time window and the DAQ rate. The cost of the new components of the trigger setup is estimated at **$20,000**.

HV supply:

The HV system of the RCS experiment, which has 900 channels of LeCroy 1461N, will be used to power the neutron detector.

DAQ:

The DAQ system built for the RCS experiment will be used for the readout of the neutron detector. This system has about 320 channels of LeCroy TDC 1877 and about 900 channels of LeCroy ADC 1881. There are over 1000 lines of RG–58 available from the connections between the RCS detector and electronics, which far exceeds the needs of the neutron detector (≈ 420).

Construction and Installation:

The collaboration will take the major part of the work on the BigBite spectrometer and the polarized He-3 target and full load of design, construction and commissioning of the neutron detector and its readout.

9 Conclusions

We request 768 hours to measure G_{En} at Q^2=1.3, 2.4 and 3.4 (GeV/c)^2 through a measurement of the cross section asymmetry of the reaction $^3\vec{H}e(\vec{e},e'n)pp$. This experiment will take place in Hall A, utilizing the BigBite spectrometer to detect electrons scattered off the Hall A polarized ^{3}He target, and an array of scintillators to detect the recoiling neutron. There are no other accurate measurements of G_{En} at these momentum transfers, and the existing data in this kinematical range, extracted from quasielastic $e-d$ scattering, have large uncertainties and are compatible with G_{En}=0 as well as with the Galster approximation. Knowledge of the neutron electric form factor G_{En} is essential for the understanding of the nucleon structure. Futhermore, it is a needed input in the analysis and interpretation of processes involving the electromagnetic interaction with nuclei. We propose to measure G_{En} to a statistical accuracy of $\Delta G_{En}/G_{En}$= 0.14, which would bring its precision to a level comparable with that of the other Sachs form factors in this kinematical regime.

The kinematics of our measurements emphasize the same Q^2 range studied for the proton in E93-027. In that experiment, it was found that the charge and magnetic current distributions in the proton are markedly different at short distances. It is an intriguing question to see if a similar tendency is duplicated in the neutron. Measuring at relatively high momentum transfers will also open additional dimensions for testing the models of the nucleon form factors in the generalized parton distribution framework.

References

[1] J.J. Kelly, arXiv:nucl-ph/0111251.

[2] M. Jones *et al.*, Phys. Rev. Lett. **84** , 1398 (2000).

[3] O. Gayou *et al.*, arXiv:nucl-ex/0111010, submitted to Phys. Rev. Lett. Nov.15, 2001.

[4] V. E. Krohn and G. R. Ringo, Phys. Rev. **148**, 1303 (1966).

[5] L. Koester, W. Nistler, and W. Waschkowski, Phys. Rev. Lett. **36**, 1021 (1976).

[6] A. Lung *et al.*, Phys. Rev. Lett. **70**, 718 (1993).

[7] S. Galster *et al.*, Nucl. Phys. **B32**, 221 (1971).

[8] N. Dombey, Rev. Mod. Phys. **41** (1969) 236.

[9] A. I. Akhiezer and M. P. Rekalo, Sov. J. Part. Nucl. **3**, 277 (1974).

[10] R. Arnold, C. Carlson, and F. Gross, Phys. Rev. **C 23**, 363 (1981).

[11] B. Blankleider and R. M. Woloshyn, Phys. Rev. **C 29**,558 (1984).

[12] R. D. McKeown, spokesperson, JLab proposal PR91-020.

[13] F. Hersman at T. Smith, spokespeople, JLab proposal PR93-037.

[14] W. Korsch and R. McKeown, spokespeople, Jlab proposal PR94-021.

[15] T. Eden *et al.*, Phys. Rev. **C50**, R1749 (1994).

[16] M. Meyerhoff *et al.*, Phys. Lett. **B327**, 201 (1994).

[17] H. Schmieden, Poc. of the 12th Int. Symposium on High–Energy Spin Physics, Amsterdam (1996), ed. by C.W. de Jager et al., World Scientific 1997, p.538.

[18] F. Klein and H. Schmieden, Nucl. Phys. **A623**, 323c (1997).

[19] F. Klein, Proc. of the 14th Int. Conf. on Particles and Nuclei, ed. by C.E. Carlson and J.J. Domingo, World Scientific 1997, p.121.

[20] M. Ostrick *et al.*, Phys. Rev. Lett. **83** 276 (1999).

[21] C. Herberg *et al.*, Eur. Phys. J. **A5**, 131 1999).

[22] I. Passchier *et al.*, Phys. Rev. Lett. **82**, 4988 (1999).

[23] D. Rohe *et al.*, Phys. Rev. Lett. **83**, 4257 (1999).

[24] H. Zhu *et al.*, arXiv:nucl-ex/0105001.

[25] J. Becker *et al.*, submitted to The Eur. Physical Journal **A**.

[26] D. Day, spokesperson, JLab proposal E93-026.

[27] R. Madey and S. Kowalski, spokespeople, Jlab proposal E93-038.

[28] R. Madey and S. Kowalski, spokespeople, JLab proposal PR01-106.

[29] M. A. Shupe *et al.*, Phys Rev **D19**, 1929 (1979).

[30] L. Andivahis *et al.*, Phys. Rev. D **50**, 5491 (1994).

[31] R. G. Arnold *et al.*, Phys. Rev. Lett. **57**, 174 (1986);
A.F. Sill *et al.*, Phys. Rev. D **48**, 29 (1993).

[32] W.K. Brooks, spokesperson, JLab proposal E94-017.

[33] S. J. Brodsky and G. Farrar, Phys. Rev. Lett. **31** (1973) 1953.

[34] S. J. Brodsky and G.P. Lepage, Phys. Rev. D **22**, 2157 (1981).

[35] X. Ji, Phys. Rev. D **55**, 7114 (1997), Phys. Rev. Lett. **78**, 610 (1997).

[36] A.V. Radyushkin, Phys. Lett. **B380**, 417 (1996).

[37] A.V. Radyushkin, Phys. Rev. **D 56**, 5524 (1997).

[38] A.V. Radyushkin, Phys. Rev. **D58**, 114008 (1998).

[39] M. Diehl, T. Feldmann, R. Jakob, P. Kroll, Eur.Phys.J. **C 8**, 409 (1999).

[40] P. Kroll, PiN Newslett. **15**, 205 (1999).

[41] K. Goeke, M. V. Polyakov, and M. Vanderhaeghen, Prog. Part. Nucl. Phys. **47**, 401 (2001).

[42] J. Ralston, P. Jain and R. Buney, Proceedings of the Conf. on Intersections of Particle and Nuclear Physics, Québec City, (2000), ed. Z. Parseh and M. Marciano, AIP Conf. Proc. No. 549 (AIP, New York, 2000), p. 302.

[43] D.B. Leinweber, R.M. Woloshyn and T. Draper, Phys. Rev. **D43**, 1659 (1991); W. Wilcox, T. Draper and K.-F. Liu, Phys. Rev. **D46**,1109 (1992); W. Wilcox, hep-lat/9608095; K.F. Liu *et al.*, Phys. Rev. **D59**, 112001 (1999).

[44] "Nuclear Theory with Lattice QCD", a proposal to DOE, N. Isgur and J.W. Negele, PI's (March 2000).

[45] T. W. Donnelly, A. S. Raskin, Ann. Phys. (N.Y.) **169**, 247 (1986).

[46] A. S. Raskin, T. W. Donnelly, Ann. Phys. (N.Y.) **191**, 78 (1989).

[47] C. Ciofi degli Atti, and S. Scopetta, Phys. Lett. **B 404**, 223 (1997).

[48] R.M. Woloshyn, Nucl. Phys. A496, 749 (1989).

[49] J. L. Friar *et al.*, Phys. Rev. **C 42**, 2310 (1991).

[50] C. Ciofi degli Atti, S. Scopetta, E. Pace and G. Salme, Phys. Rev. **C48**, 968 (1993).

[51] R.W. Schulze and P.U. Sauer, Phys. Rev. **C56** 2293 (1997).

[52] F. Bissey, A.W. Thomas, and I.R. Afnan, Phys. Rev. **C64**, 024004 (2001).

[53] R.W. Schulze, P.U. Sauer, Phys. Rev. **C 48**, 38 (1993).

[54] D. Higinbotham, http://hallaweb.jlab.org/equipment/BigBite/index.html.

[55] D. J. J. de Lange *et al.*, Nucl. Instr. and Meth. **A 406**, 182 (1998).

[56] D. J. J. de Lange *et al.*, Nucl. Instr. and Meth. **A 412**, 254 (1998).

[57] V. Nelyubin, private communication.

[58] P.V. Degtyarenko, "Applications of the Photonuclear Fragmentation Model to Radiation Protection Problems", Proceedings of the Second Specialist's Meeting on Shielding Aspects of Accelerators, Targets and Irradiation Facilities (SATIF2), 12-13 October 1995, CERN, Geneva, Switzerland, p. 67; P.V. Degtyarenko, M.V. Kossov, H-P. Wellisch, Chiral Invariant Phase Space Event Generator, I. Nucleon-antinucleon annihilation at rest, Eur. Phys. J. A **8**, p. 217 (2000).

[59] H. R. Poolman *et al.*, Nucl. Instr. and Meth. **A 439**, 91 (200).

[60] T. Blaich *et al.*, Nucl. Instr. and Meth. **A 314**, 136 (1992).

[61] J. Annand *et al.*, Nucl. Instr. and Meth. **A 262**, 329 (1987).

[62] B. Wojtsekhowski, P. Degtyarenko, R. Lindgren, "A New Tool For Correlation Studies in Hall A at JLAB, JLab-TN-01-047", report on 5th Workshop on Electromagnetically Induced Two-Hadron Emission, Lund, Sweden, (2001).

[63] M. M. Sargsian, arXiv:nucl-th/0110053 and private communication.

[64] J. M. Udias, private communication.

[65] J. M. Laget, private communication.

[66] R.L. Jaffe, F.E. Close, R.G. Roberts and G.G. Ross: Phys. Lett. **B134**, 449 (1984).

[67] L.L. Frankfurt and M.I. Strikman: Nucl. Phys. **B250** (1985) 143.

[68] D. F. Geesaman, K. Saito and A. W. Thomas, Ann. Rev. Nucl. Part. Sci. **45**, 337 (1995).

[69] G. A. Miller and J. R. Smith, arXiv:nucl-th/0107026.

[70] L. L. Frankfurt, G. A. Miller and M. Strikman, Ann. Rev. Nucl. Part. Sci. **44**, 501 (1994).

[71] K. Garrow *et al.*, arXiv:hep-ex/0109027.

[72] S. Dieterich *et al.*, Phys. Lett. **B 500**, 47 (2001).

[73] S. Dieterich, private communication.

[74] J. M. Laget, Phys. Lett. **B 273**, 367 (1991).

[75] C.Ciofi degli Atti, E. Pace, G. Salme, Phys. Rev. **C 51**, 1108 (1995).

[76] J. Golak it et al., arXiv:nucl-th/0110060.

[77] C. Ciofi Degli Atti and L. P. Kaptari, arXiv:nucl-th/0110062.

[78] L.D. Faddeev, *Mathematical Aspects of the Three-Body Problem* (Daniel Davey and Co., Inc., New York, 1965).

[79] R.M. Woloshyn, Nucl. Phys. A496, 749 (1989).

[80] R. Niyazov and L. Weinstein, private communication.

[81] D. Higinbotham, private communication.